Evolution of Turbulent Boundary Conditions on the Surface of Large Barchan Dunes: Anomalies in Aerodynamic Roughness and Shear Velocity, Aeolian Threshold, and the Role of Dune Skewness

M. Louge, A. Valance, J. Fang, S. Harnett, F. Porté-Agel, Patrick Chasle

JGR Earth Surface

Key Points:

- At the brink of a mature barchan, theory, simulations and field data reveal a peak of shear stress rising with dune skewness
- Aerodynamic roughness on dunes with rocky surroundings disagree with Nikuradse's (1933, https://ntrs.nasa.gov/citations/19930093938) data for fully developed turbulent boundary layers
- We discuss challenges that large-eddy simulations face to reproduce turbulent flow on field-size dunes

Correspondence to:

A. Valance,
Alexandre.Valance@univ-rennes1.fr

Author Contributions:

Conceptualization: M. Y. Louge, A. Valance, S. J. Harnett
Data curation: M. Y. Louge, A. Valance, J. Fang, F. Porté-Agel
Formal analysis: M. Y. Louge, A. Valance
Funding acquisition: M. Y. Louge
Investigation: M. Y. Louge, A. Valance, S. J. Harnett, P. Chasle
Methodology: M. Y. Louge, A. Valance, S. J. Harnett, P. Chasle

Evolution of Turbulent Boundary Conditions on the Surface of Large Barchan Dunes: Anomalies in Aerodynamic Roughness and Shear Velocity, Aeolian Threshold, and the Role of Dune Skewness

M. Y. Louge[1] , **A. Valance[2]** , **J. Fang[3]** , **S. J. Harnett[1]** , **F. Porté-Agel[3]**, and **P. Chasle[2]**

[1]Sibley School of Mechanical and Aerospace Engineering, Cornell University, Ithaca, NY, USA, [2]Institut de Physique de Rennes, Université de Rennes 1, Rennes, France, [3]École Polytechnique Fédérale de Lausanne, Lausanne, Switzerland

Abstract We recorded aerodynamic roughness and shear velocity along transects on and around mature crescent-shaped barchan dunes of 4.5 m and 27 m height above the horizontal rock-covered Qatar desert by fitting to the log-law time-averaged vertical velocity profiles acquired from triads of ultrasonic anemometers penetrating the inner turbulent boundary layer. Shear velocity first decreased, then recovered as air climbed on the dune, with a local maximum ahead of the crest as predicted by the Jackson and Hunt (1975, https://doi.org/10.1002/qj.49710143015) theory. Unlike flows over gentler bedforms without a slope discontinuity, an anomalous peak of shear velocity also arose on the dune centerline at the brink, which the theory attributed to skewness in the dune transect profile. The onset of aeolian transport produced a log-law passing through the Bagnold (1941, https://doi.org/10.1007/978-94-009-5682-7) focal point. It was bracketed by noticeable hysteretic peaks in the correlation between wind speed and entrained sand flux. The dunes' rocky surroundings and topography produced an aerodynamic roughness at odds with the Nikuradse (1933, https://ntrs.nasa.gov/citations/19930093938) data for fully developed turbulent boundary layers. Large-eddy numerical simulations illustrated the sensitivity of shear velocity to wide changes in aerodynamic roughness from desert floor to dune surface.

Plain Language Summary Wind friction is the engine that erodes sand dunes, relentlessly pushing them over roads, houses, and infrastructure. Our records of wind speed on crescent-shaped mobile dunes challenge the conventional understanding of this process. Comparing field measurements and models, we show that the highest friction occurs where the gentle upward dune surface abruptly gives way to a steeper avalanching downward slope. Our data also reveals that the "aerodynamic roughness," a measure of wind friction on sand, is at odds with historical data meant for turbulent pipe flow. Because numerical simulations are used to predict flow over landforms that are inaccessible to detailed measurements, we validate them against data on a large dune. Our observations imply that, to achieve greater fidelity, simulations should subdivide the fluid neighborhood of the dune more finely, and revisit how they treat aerodynamic friction on its surface. Although our work involved large desert dunes, we expect these suggestions to apply more broadly to atmospheric, fluvial or submarine landforms that are surrounded by rougher terrain or that feature sudden changes in slope.

1. Introduction

Aeolian transport determines the size, shape and speed of crescent-shaped "barchan" sand dunes forming on a hard, relatively flat desert floor (Andreotti et al., 2002). When upstream sand availability is limited (Lü et al., 2018), their initial growth involves two simultaneous mechanisms (Kroy et al., 2002). First, as Jackson and Hunt (1975) and Hunt et al. (1988) predicted for a low bedform, the basal shear stress $\tau \equiv \rho u^{*2}$ on sand, or its shear velocity u^*, reach a maximum *ahead* of the dune crest, as the inertia of air with density ρ within the "inner layer" near the surface compels the peak wind speed in the outer flow above the crest to lag behind the forcing imposed by τ (Charru et al., 2013; Fourrière et al., 2010).

Second, Sauermann et al. (2001) recognized that grain inertia gives rise to a "saturation length" delaying the strongest aeolian transport flux from where τ peaks. In this reasoning, the two mechanisms cooperate to enlarge the dune: although the peak shear stress occurs upwind of the highest dune elevation, fluid inertia displaces its

effect on aeolian transport downwind, while the saturation length delays sand accumulation (Durán et al., 2011). In this hypothetical mechanism, the dune thus grows until the saturation length becomes equal to the distance between the peaks of stress and topography, at which point the whole bedform reaches a mature equilibrium size.

Models of whole dune fields (Lü et al., 2018; Narteau et al., 2009; Xiao et al., 2023; D. Zhang et al., 2010, 2012) and studies of dunes reversing direction (N. S. Chen et al., 2022; Gao et al., 2021) also invoke the theory of Jackson and Hunt (1975) as they assume that the increment in shear stress over its counterpart on a flat surface is proportional to dune slope. However, for simplicity, they ignore the prediction that variations in shear stress along the wind lead those in topography.

Large-eddy-simulations (LES) over relatively large domains (Hardy et al., 2021) and Reynolds-averaged-Navier-Stokes (RANS) models (Jin et al., 2021) similarly disregard such lead of shear stress over topography. To avoid resolving the relatively thin "inner layer" of Jackson and Hunt (1975), they apply instead the boundary conditions of Launder and Spalding (1974) to the surface, which amounts to adopting an aerodynamic roughness and pegging basal shear stress to overhead wind speed. As our observations will reveal, this simplification prevents simulations from capturing important details of stress variations on a real dune.

Although barchans have moderate enough upwind slopes to uphold the linear assumptions of Jackson and Hunt (1975), their sharp topographical change at the "brink" challenges the theory. There, the windward smooth surface abruptly gives way to a much steeper incline descending near the angle of repose (Allen, 1970; Louge et al., 2015). To handle this discontinuity in the linear framework of the theory, Kroy et al. (2002) extrapolated the windward surface above the separation bubble to treat the dune wake as a virtual object over which wind streamlines glide more evenly. In other words, Kroy et al. (2002) effectively suppressed the negative skewness characterizing the profile of mobile dunes possessing an avalanche face. Doing so, their application of the Jackson and Hunt (1975) theory predicted smooth variations of shear stress leading the dune topography. Durán et al. (2010) adopted this treatment to elucidate the formation of entire dune fields with some success.

However, on a mature desert barchan featuring an avalanching lee, our field anemometry discerned a sharp peak in turbulent shear velocity u^* just upwind of the brink. Such anomaly was not observed on a sand heap with smoother topographical variations (Claudin et al., 2013), but it appeared in much smaller barchans forming in a water flume (Charru & Franklin, 2012). Although the linear theory of Jackson and Hunt (1975) was not designed to handle sharp discontinuities, we find nonetheless that its integration over the recorded topography also features a peak of shear stress at the brink, and that the strength of this peak grows with skewness magnitude of the dune transect along the wind.

Our measurements of shear velocity u^* and "aerodynamic roughness" z_0 over mature barchans complement the field work of Weaver and Wiggs (2011) and A. B. Smith et al. (2017) by reporting how the turbulent boundary layer gradually transitions from a desert floor littered with rocks of 5–30 cm size to the much smoother erodible dune surface. Perhaps our most significant contribution is the observation of ln z_0 values that disagree widely with experiments of Nikuradse (1933) for fully developed turbulent flows in pipes roughened with sand grains. More broadly, Nikuradse's results are often invoked to posit aerodynamic roughness in geophysical turbulent flows, rather than to measure its evolution in situ, or to predict it from direct numerical simulations. For example, in fluvial environments, ln z_0 is implicitly related to the Chézy correlation of basal shear stress and mean flow speed (D'Ippolito et al., 2021; Lefebvre et al., 2014). Our observations imply that such practice is arbitrary.

Lastly, we used an acoustic probe to measure the flux of sand that wind transported near the crest. Although we did not deploy this probe elsewhere on the dune, our observations of a greater local shear velocity at the brink suggest that the rate of aeolian erosion feeding the dune's downwind avalanche face may be more intense than inferred from existing aerodynamic models. Three distinct hysteretic peaks in the time-correlation of sand flux and wind strength bracketed the aeolian transport speed threshold of Bagnold (1941), above which shear velocity and aerodynamic roughness abruptly change as air momentum is depleted by the presence of lifted sands. We also examined why existing correlations inspired by Shields (1936) overpredicted the threshold stress required to mobilize our sands, and suggested that the discrepancy may be inherited from the greater bumpiness of the surrounding desert floor.

The present contribution is the last in a series of articles on this Qatar desert, which concerned heat transfer inside the small barchan (Louge et al., 2013), microbiota of the dune field (Abdul-Majid et al., 2016), remote sensing of

its motion (Michel et al., 2018), vapor transport and respiration across the sand surface, internal evanescent waves of moisture, and interactions with the atmospheric boundary layer (Louge et al., 2022).

We begin this article with a description of field anemometry. After verifying that the log-law for the core of a turbulent boundary layer adequately captures wind speed profiles above the surface at all times and locations on and around the dunes, we show that anomalously high values of u^* exist at the brink. Having recorded the dune topography, we then compare these observations with the LES and with predictions of the Jackson and Hunt (1975) theory, as implemented by Weng et al. (1991), Kroy et al. (2002), and Walmsley et al. (1986). Finally, our anemometry confirms that the Bagnold (1941) focal point conjecture captures variations of z_0 and u^* once transport occurs, but it suggests that correlations for local shear threshold inspired by Shields (1936) are corrupted by distant changes in surface bumpiness.

2. Field Measurements

We conducted anemometry and aeolian transport measurements on 10–16 January 2017 on a relatively small barchan with 60 m toe-to-brink distance, 80 m horn-to-horn, and $h_{max} \simeq 4.5$ m crest elevation above a relatively rough rock-covered Qatar desert ground near El-Kharrara at $25° 00' 30''$ N, $51° 20' 27''$ E, while wind blew toward an average bearing of $141°$ close to the $159°$ historical direction of this mobile dune. We also studied a much larger barchan on 30 April to 3 May 2017 at $25° 00' 45''$ N, $51° 19' 58''$ E with 145 m toe-to-brink distance, 440 m horn-to-horn, and 27 m peak elevation.

Sands on the upwind face of barchans in this desert have a material density $\rho_s \simeq 2630$ kg/m^3, and moments of the particle-size-distribution by mass $\bar{d} \simeq 351$ μm, $d_{20} \equiv \left(\overline{d^2}\right)^{1/2} \simeq 365$ μm, and $d_{30} \equiv \left(\overline{d^3}\right)^{1/3} \simeq 377$ μm, where the overbar denotes averaging over the PSD and indices are consistent with the notation of Babinsky and Sojka (2002), summarized in Appendix B of Louge et al. (2022). To compare with aeolian transport results of Zhu et al. (2019), our PSD also features $d_{v10} = 123.4 \pm 9.2$ μm, $d_{v50} = 307.2 \pm 5.3$ μm, and $d_{v90} = 456.8 \pm 3.8$ μm, which represent the diameters below which 10%, 50% and 90% of solid volume reside, respectively.

We deployed three separate triads of Gill Instruments Windsonic ultrasonic anemometers of 142 mm diameter, each consisting of two parallel plates separated by 82 mm, yielding wind speed and direction with 0.01 m/s resolution, 0 to 60 m/s speed range and angular accuracy $\pm 3°$. For each triad, anemometers were attached to a frame of PVC tubes oriented to avoid interference with the wind stream. A battery-powered Campbell Scientific CR-800 digital portable data acquisition card recorded speed and direction at intervals $\leqslant 3$ s. A Leica TS02 theodolite recorded the precise Easting, Northing and Height of each anemometer in the roving triad using a field mini-prism, thereby allowing us to calculate the normal unit vector $\hat{n}$ to the dune surface and absolute wind velocity vectors at each location. We also used the theodolite to survey dune size and shape.

Figure 1 shows setup details and anemometer locations on the small dune. Two triads were installed at fixed positions to acquire data continuously over the entire campaign, one sufficiently upwind to record conditions on the desert floor, and the other higher on the dune. The third triad was "roving," in that its three anemometers were attached to a rigid tube frame that could be transported with relative ease to many locations on and around the dune, and then be left to record wind speed and direction continuously over time intervals no shorter than 15 min. To avoid data corruption, the roving triad was positioned outside the wake of its fixed counterparts, and data from all three triads was discarded from at least 1 min before, during and after its placement. In this way, the roving anemometers let us chart variations of shear velocity and aerodynamic roughness along several dune transects. On one occasion, the roving triad also acquired data at a distance of 0.92 m from the brink over 17.5 hr, while the triads fixed to the dune and desert floor operated simultaneously for comparison.

Finally, to evaluate the threshold wind velocity at which sand transport began and ended, we deployed the acoustic probe that Ahmedou et al. (2007) used in Mauritania and calibrated in a wind tunnel. The probe consisted of a 50 cm-tall vertical aluminum tube of 2 cm diameter positioned just above the surface to be struck by most transported sand grains (Figure 1b).

3. Turbulent Boundary Layer

For context, we first discuss general characteristics of the turbulent boundary layer. We show that all recorded vertical profiles conformed to the log law in its core. Then, we outline how vertical anemometer elevations were
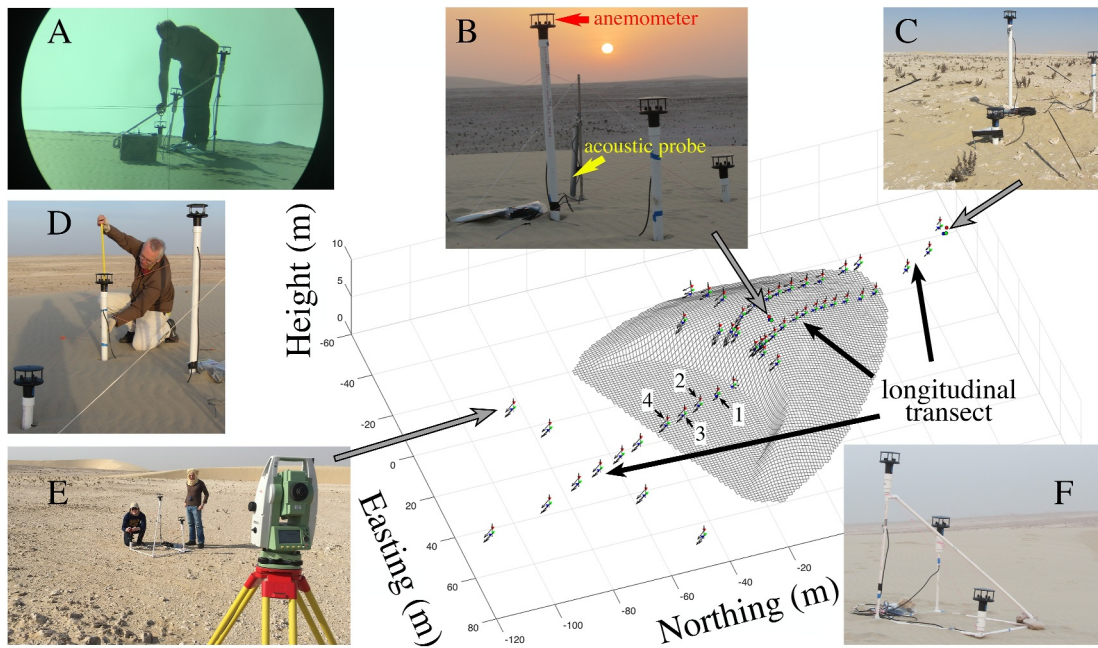
Figure 1. Anemometry on the small dune at $25° 00' 30'' N, 51° 20' 27'' E$. Easting, Northing, and Height (ENH) (m) are relative to the barycenter of the dune outline on the desert floor, which is made horizontal by tilting its normal vector by $+0.28°$, $-0.06°$ and $-0.29°$ to account for slight ground inclination along the ENH directions. Once magnified, blue, green, and red symbols represent low, medium and high anemometers; circles are fixed anemometers upwind and on the dune; triangles show successive roving triads; arrows indicate mean wind speed and direction; numbers 1–4 mark roving locations seen in Figures 3, 5, and 13. (a) Viewed through the theodolite reticle, a fix on one of the anemometers using the mini-prism. (b) Fixed anemometer triad on the dune and acoustic probe. (c) Fixed triad upwind. (d) Checking anemometer elevation. (e) Roving triad on rock-covered ground behind the small "Nadine" dune, with the larger "Chris" dune in the background, and (f) on the dune.

selected to penetrate the "inner" region just above the dune surface, in which fluid inertia causes the basal shear stress τ to lead the wind velocity u as it accelerates over the dune. Next, we justify why thermal instabilities of the atmospheric boundary layer, while important farther aloft, barely affected turbulent profiles at the relatively low elevations of our anemometers. Lastly, we indicate how small wind speeds, which occur mostly at night, produce a meandering flow that does not conform to the classical view of a turbulent core.

The turbulent boundary layer above a flat plate includes a viscous sublayer, a buffer, and a turbulent "core" with velocity u satisfying

$$u/u^* \simeq a_u + (1/\kappa)\ln(zu^*/\nu),\tag{1}$$

where $\kappa \simeq 0.41$ is von Kármán's constant, $\nu \simeq 1.5\ 10^{-5}\ \mathrm{m^2/s}$ is the kinematic viscosity of air (Kays & Crawford, 1980), and z is elevation above the surface. Our ultrasonic anemometers were too thick to resolve the viscous and buffer layers. For example, if the surface was smooth, the transition between buffer layer and core would occur at the altitude $z_t \simeq 30\nu/u^*$. Therefore, with typical $u^* \gtrsim 0.1$ m/s in the field, our instruments could not possibly fit within $z_t \lesssim 5$ mm. Instead, the design of our triads was a compromise between portability, vertical resolution and redundancy. Its aim was to determine values of u^* and z_0 arising in the "log-law of the wall," which serves as an alternative to Equation 1 for the core of the turbulent boundary layer

$$u/u^* = (1/\kappa)\ln(z/z_0).\tag{2}$$

By fitting u^* and z_0 to measured values of u at three known elevations, this method offered minimum redundancy for checking whether Equation 2 correctly captured the turbulent profile. Eliminating u/u^* from Equations 1 and 2 yields

$$\ln(u^* z_0/\nu) = -a_u\ \kappa.\tag{3}$$

For smooth walls, $a_u = a_{u_0}$ is constant (Saph & Schoder, 1903). Without asperities, z_0 is not a geometrical length scale, but it originates from upstream coherent structures (Wu & Moin, 2009). More generally, as Section 7 will discuss, z_0 on our evolving dune bedform is severely affected by the nature of the desert floor upstream.

When u^* rises with the mean Reynolds number, Nikuradse (1933) showed that $\ln z_0$ does not decrease indefinitely in rough pipes, but that it reaches instead an asymptotic geometrical value set by the diameter of sand grains that he glued to the pipe's inside surface. By least-squares fitting the nearly invariant Darcy friction factor at the highest Reynolds number of his experiments, one obtains the classical result for a rough wall in the limit of large u^*,

$$z_0 = z_{0_\infty} \equiv \bar{d}/\varpi, \tag{4}$$

where $\bar{d}$ is the average grain diameter, and $\varpi = 34.6 \pm 0.3$. Because $\bar{d}/\varpi$ and u^* are the only local scales of distance and speed in a fully developed turbulent boundary layer of indefinite extent, it is natural to define the Reynolds number $\mathrm{Re}^* \equiv u^* z_{0_\infty}/\nu$ and the dimensionless turbulent roughness $z_0^\dagger \equiv z_0/z_{0_\infty}$, such that $\ln z_0^\dagger \to 0$ as $\ln \mathrm{Re}^* \to \infty$.

For turbulent flows climbing over gentle topography, Jackson and Hunt (1975) recognized that, in the streamwise direction, fluid inertia in an "inner layer" just above a bedform delays the response of wind velocity u to changes in basal shear stress along its surface. Specifically, the basal shear stress $\tau = \rho u^{*2}$ on a dune is not highest where wind speed aloft peaks over its crest, but instead τ (or u^*) are maximum ahead of it. From a balance of acceleration and shear stress gradient terms in their streamwise momentum Equation 2.10a, and by fixing coefficients of their leading order as unity, Jackson and Hunt (1975) estimated the thickness ℓ of the inner layer where such delay occurs as

$$\frac{\ell}{2\lambda\kappa^2}\ln^n\!\left(\frac{\ell}{z_0}\right) \sim O(1), \tag{5}$$

with exponent $n = 1$. Weng et al. (1991) and Sauermann et al. (2003) adopted this expression for measurements of wind speed and sand transport over a barchan dune.

Later, by adopting a dependence on $\ln z$ of the difference Δu between the upstream velocity profile and that over the hill, Taylor et al. (1987) suggested another scaling with $n = 2$, which produces much thinner estimates of ℓ from Equation 5. Nonetheless, as Taylor et al. (1987) recognized in their Section 4.1, the inner layer thickness is challenging to pin down with certainty. To compare their new prediction with data, they identified ℓ as the altitude where Δu is maximum. Then, they found that $n = 2$ better captured measurements estimates of ℓ than $n = 1$ for four out of six available data sets summarized in their Table II. For a smooth bedform of wavelength $\lambda \simeq 46$ m and aerodynamic roughness $z_0 \simeq 12$ μm, Claudin et al. (2013) chose $n = 2$, which yields $\ell \simeq 18$ cm. Inspired by their anemometer placement, we located the midpoints of our instruments at the same relative elevations $z_1 \simeq 29$ cm, $z_2 \simeq 73$ cm, and $z_3 \simeq 115$ cm above the sand surface.

Interpreting λ as twice the toe-to-brink distance L of our dunes, Equation 5 yields estimates of $\ell \simeq 40$ cm and 110 cm with $n = 2$ for our small and large barchans, respectively, while $n = 1$ produces much larger values $\ell \simeq 3.5$ m and 10.6 m. In other words, adopting $n = 2$ would imply that only our lowest anemometer resides in the inner layer on the small dune, whereas the original scaling of Jackson and Hunt (1975) places them all well within it.

Meanwhile, as Figure 2 illustrates, time-averaged velocity profiles closely conformed to the logarithmic profile in Equation 2. To quantify this at all anemometer locations, we derived an error bar for u^* as a 80% confidence interval for the slope of the linear regression of u versus $\ln z$ using Student's t-distribution (Louge et al., 2023). In all cases, the value of u^* derived from only the lower two anemometers was within the error bar of u^* obtained with all three. This suggests that the logarithmic profile extended at least to the top anemometer. Therefore, it is likely that the actual thickness of our inner layer was comprised between the relatively low value predicted by Taylor et al. (1987) with $n = 2$ and its much thicker counterpart from Jackson and Hunt (1975) with $n = 1$. A definitive resolution of this question will require anemometry of finer resolution reaching both lower and higher altitudes than our own.
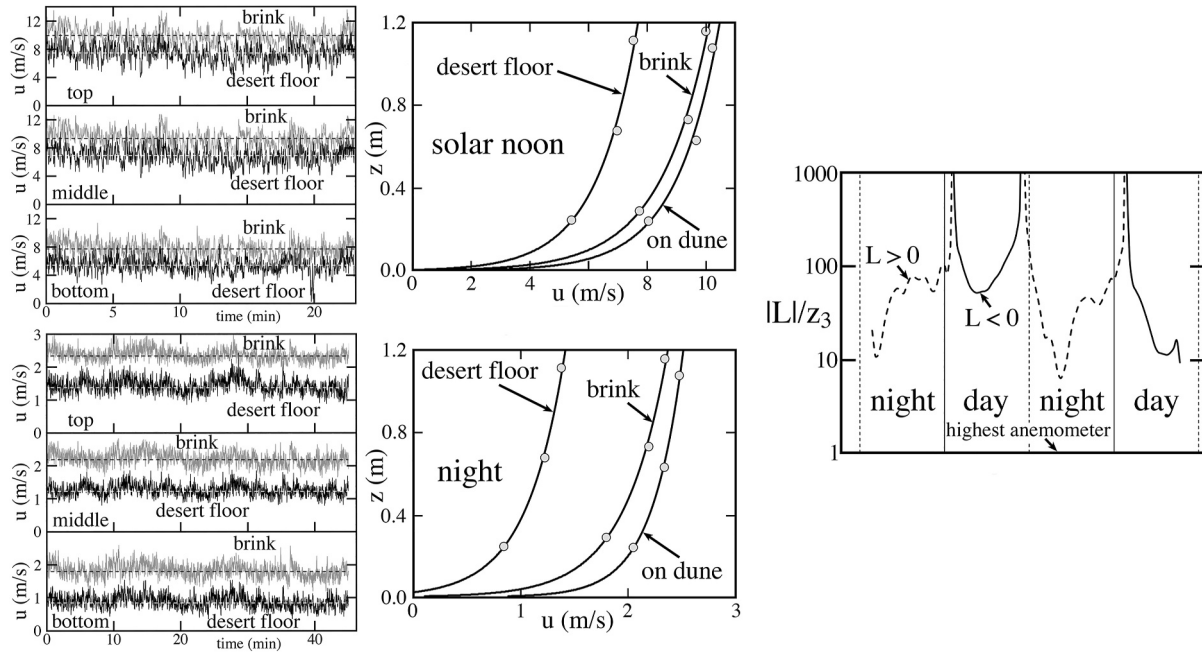
Figure 2. Left graphs: instantaneous wind speed parallel to the surface at the bottom, middle and top anemometers of the roving triad deployed at a 0.92 m distance from the brink and at the fixed triad on hard desert floor upstream of the small barchan. Middle graphs: the corresponding simultaneous time-averaged vertical wind profiles near the brink and on the desert floor, as well as at the fixed anemometer triad on the dune (placement, see Figure 1b). Top and bottom graphs are respectively recorded around solar noon and 4 hr after sunset. Right graph: Monin-Obukhov length estimated from measurements of Louge et al. (2013) on 19–21 March 2011. Vertical solid and dashed lines mark sunrises and sunsets. Negative values of L are shown as solid lines; positive as dashed lines.

In the desert, another complication arises from possible interactions with the thermal boundary layer. However, as Figure 2 indicates, such effect is inconsequential. In the presence of significant vertical temperature gradients, wind profiles are subject to the Monin-Obukhov similarity

$$\frac{\kappa z}{u^*} \frac{\partial u}{\partial z} = \varphi. \tag{6}$$

Without thermal gradients, φ equals one, thus leading to Equation 2. In their presence, experiments conducted in Kansas at much higher elevations suggested instead

$$\varphi \simeq (1 - a_D \, z/L)^{-1/4} \tag{7}$$

when the atmospheric boundary layer is unstable during the day, and

$$\varphi \simeq 1 + a_N \, z/L \tag{8}$$

when buoyancy suppresses turbulent velocity fluctuations at night (Haugen et al., 1971). Fitted constants are approximately $a_D \simeq 15$ and $a_N \simeq 4.8$ (Wyngaard, 2010). The Monin-Obukhov length

$$L \equiv \frac{u^{*3} \, \rho c_p T}{\kappa \, g \, \dot{q}''}, \tag{9}$$

is a measure of the scale of the corresponding distortions. Here, T is absolute air temperature, g is gravitational acceleration, and $\dot{q}'' \propto \partial T/\partial z$ is the convective heat flux at the surface, typically negative during the day when sand loses heat, and positive at night when the ground is colder than the air aloft.
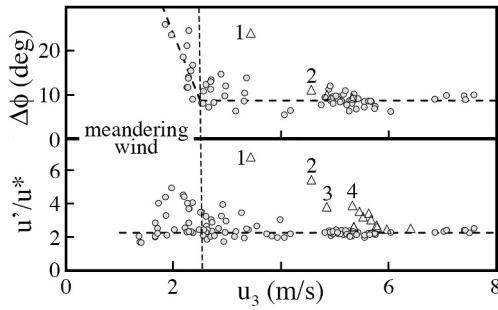
Figure 3. Meandering upstream at low wind and in the wake. Top graph: circles are rms fluctuations $\Delta\phi$ in wind direction versus speed u_3 at the top anemometer of the triad on the hard desert floor upstream of the dune (placement, see Figure 1c). The horizontal dashed line is the average $\Delta\phi \simeq 9°$ for $u_3 > 4$ m/s. The vertical dashed line marks the transition $u_3 \simeq 2.5$ m/s below which the wind exhibits meandering behavior. Bottom graph: circles are ratios of recorded speed fluctuations u' in the plane of the top anemometer relative to the shear velocity u^* fitted for this fixed upstream triad. The horizontal dashed line marks the constant $(2/3)^{1/2}\chi$ from Equation 10. Numbered triangles are roving anemometer downwind of the dune (locations shown in Figure 1).

A definitive determination of L requires knowledge of wind speed u^*, as well as temperatures at the sand surface and in the atmospheric boundary layer at one or more altitudes. Although we did not record such temperatures in this campaign, typical values of L can be estimated from earlier measurements on the same dune, documented by Louge et al. (2013, 2022) and their supporting information. The right panel of Figure 2 shows the time-history of $|L|$ over two typical days. As expected, inverted stable thermal boundary layers arose at night, then gave way to instabilities shortly after sunrise and before sunset. In all cases, $|L|$ was much greater than the altitude z_3 of our highest anemometer, thereby maintaining φ close to unity in the elevation range that we examined.

Consistent with these estimates, the middle panels of Figure 2 show that vertical profiles of mean wind speed conformed to Equation 2 without distortion at night or high noon. In this context, we simply assume that, if φ differed slightly from unity, its value was the same at all locations on or around the dune. Then, for a given time-average interval >15 min, forming the ratio of u^* at a roving location to that at the fixed anemometer on the dune allows relative comparisons of shear velocity along transects that are nearly independent of mean wind speed or thermal conditions.

Nonetheless, such comparisons can be more uncertain at low wind speeds. As Anfossi et al. (2005) suggested, wind can meander when $u \lesssim 2$ m/s. For faster flows in isotropic turbulence, fluctuation velocities produce a normal stress $\sigma_{xx} = \sigma_{yy} = \sigma_{zz} = (\rho/3)\left(u_x'^2 + u_y'^2 + u_z'^2\right)$ that is related to the shear velocity through $\sigma \simeq (\rho/3)\chi^2 u^{*2}$, where $\chi \simeq 2.75 \pm 0.25$ (Fourrière et al., 2010). Because our anemometers only recorded two-dimensional resultant speed fluctuations $u' \equiv \left(u_x'^2 + u_y'^2\right)^{1/2} \simeq (2/3)^{1/2}\left(u_x'^2 + u_y'^2 + u_z'^2\right)^{1/2}$ on a plane parallel to the base, we therefore expected these fluctuations to be related to the fitted shear velocity u^* through

$$\frac{u'}{u^*} \simeq \left(\frac{2}{3}\right)^{1/2}\chi. \tag{10}$$

As Figure 3 shows, this relation was upheld when the wind speed u_3 recorded by our highest anemometer on the desert floor exceeded approximately 2.5 m/s. Below this value, the wind meandered with directional rms fluctuations $\Delta\phi$ rising above the 9° that we normally recorded with stronger winds. Because such meandering complicates turbulence modeling, we identify in this article conditions when it may have occurred (e.g., open circles in Figure 5).

Nonetheless, as the next section discusses, time-averaged velocities recorded at three elevations conformed well to the log-law at all anemometer stations, even at low winds or, surprisingly, behind the dune (Figure 4).

4. Transects of Shear Velocity

Figure 5 shows dune topography and evolution of shear velocity u^* along the main streamwise longitudinal transect identified in Figure 1. Because mean wind strength rose and fell in unison along the entire transect, Figure 5 presents the ratio of u^* at the roving triad relative to its value u_r^* at the fixed triad on the dune. This reference selection of u_r^* was natural since sand aerodynamic roughness is typically smaller than on the surrounding desert floor.
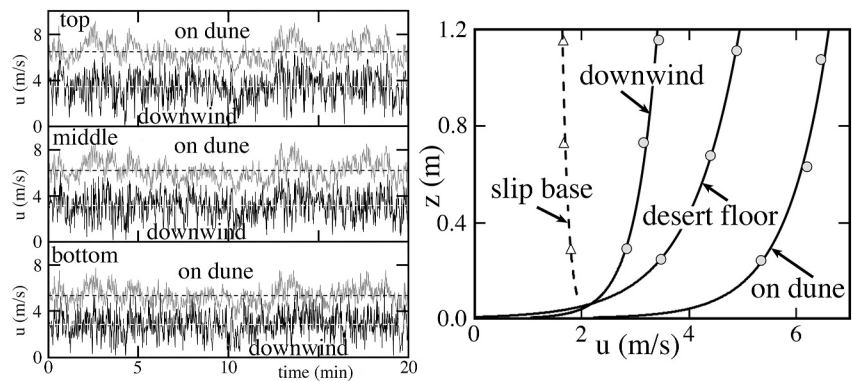
Figure 5 qualitatively confirms predictions of the Jackson and Hunt (1975) theory. Along the wind direction, u^*/u_r^* first decreases, then rises to a local maximum ahead of the crest. Theory predicts that the distance between this local maximum and the crest is $(\lambda/2\pi)B/A$ (Kiki-Sandoungout, 2019), where λ is the dominant wavelength of a bedform shaped as a cosine, and A and B are coefficients that Fourrière et al. (2010) calculated in terms of the dimensionless surface roughness $\eta_0 \equiv 2\pi z_0/\lambda$, and provided in their supporting information as convenient fits in terms of $R \equiv -\ln(z_0/\lambda) > 0$, valid for $\eta_0 \lesssim 10^{-3}$, see also Musa et al. (2014) (For a Lorentzian profile, Kroy et al. (2002) found the similar expression $(\lambda/3\pi)B/A$, see their footnote [12]). With an average $z_0 \simeq 100$ μm

Figure 4. Left: instantaneous wind speeds at the bottom, middle, and top anemometers deployed at the fixed dune location (placement, see Figure 1b) and at the roving triad on point 1 located 7.2 m "downwind" of the base of the avalanche face. Right: solid lines are least-squares fits to simultaneous vertical profiles of time-average velocity for these triads, along with the fixed triad on the hard desert floor. The dashed line is a similar fit for the roving triad at a distance <0.5 m downstream from the base of the slip face with an exceptional reversal $u^* \simeq -0.45$ m/s.

recorded near the crest and $\lambda \simeq 90$ m taken as twice the distance between toe and crest on the transect, $A \simeq 3.9$, $B \simeq 1.4$ and $(\lambda/2\pi)B/A \simeq 5$ m, which is consistent with the recorded 6.8 m distance between the local maximum of u^*/u_r^* and the crest.

A feature of this transect is the peak of u^*/u_r^* recorded at the relatively short 0.92 m distance upstream of the brink. There, in the absence of aeolian transport or wind reversal, we found $u^*/u_r^* = 1.21 \pm 0.04$ at 80% confidence from a long-term record subdivided in 37 intervals of 20 min (circle and error bar labeled "brink" in Figure 5). Charru and Franklin (2012) also reported such peak at the brink of small barchan dunes forming in a water flume. These observations may be related to the increased turbulence that Weaver and Wiggs (2011) recorded between brink and crest (their Figure 11 at an altitude of 0.3 m), or perhaps to the increased "speed-up ratio" that Michelsen et al. (2015) discerned in 2d and 3d RANS simulations. As Section 9 will show, invoking the existence of a separating streamline acting as the solidified upper boundary of a separation bubble downstream of the brink effectively suppresses this anomalous peak in shear velocity.

To examine whether such bubble exists, we placed the roving triad at several locations behind the dune. The first intriguing observation was the profile recorded just behind the downwind avalanche face, which we show as a dashed line in Figure 4. A close look at Figure 1 reveals that the mean wind velocity at this roving triad had a bearing 41° nearly parallel to the avalanche face, while the negative $u^*/u_r^* \simeq -0.14$ implied a flow reversal of the turbulent boundary layer at the sand surface. Beside this exceptional point, all roving triads behind the dune recorded mean velocities aligned with the prevailing wind direction, and they all conformed to the log-law, see for
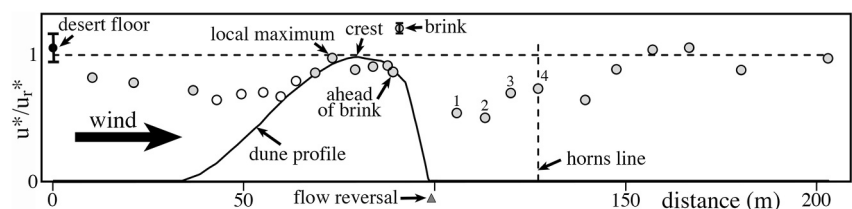
Figure 5. Shear velocity u^* measured with the roving triad relative to its simultaneous reference value u_r^* from the fixed triad on the dune versus distance along the path labeled "longitudinal transect" in Figure 1, acquired in 17 to 23 min time intervals. The dark circle on the desert floor and its error bar are calculated from eight records lasting 1 hr, during which wind blew to a bearing of $139 \pm 5°$ and was neither meandering nor reversing course. Open circles indicate data acquired with $u_3 < 2.5$ m/s at the top roving anemometer. The largest u^*/u_r^* was acquired at 0.92 m ahead of the brink. The triangle at $u^*/u_r^* \simeq -0.14$ is the only flow reversal that we observed just behind the base of the avalanche face. Points labeled 1 through 4 are located behind the dune, as shown in Figures 1 and 3. The vertical dashed line marks the line joining the downwind tips of the two dune horns. The horizontal one is $u^*/u_r^* = 1$. The solid line is dune surface elevation versus distance relative to crest altitude, magnified for clarity.
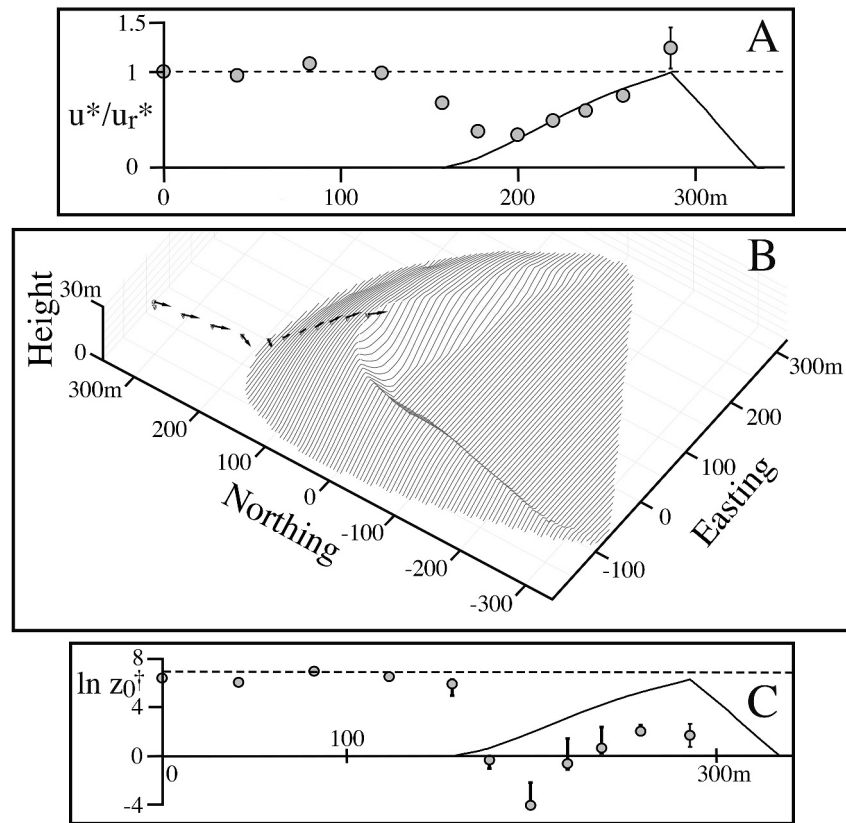
Figure 6. Anemometry on the larger dune of 27.2 m peak height. (a) Profile of u^*/u_r^* along the transect shown in (b), with origin at the fixed triad on the rough desert floor. The error bar at the brink is calculated from 10 records of 20 min at 80% confidence. The dashed line marks $u^* = u_r^*$. (b) Dune topography with superimposed roving anemometer positions and arrows $\propto u^*/u_r^*$ aligned with the wind velocity. (c) Profile of $\ln z_0^\dagger \equiv \ln(z_0/z_{0_\infty})$ along the transect with error bars discussed in Section 7. The dashed horizontal straight line is $\ln z_0^\dagger \simeq 6.9$ from Louge et al. (2013). In panels (a) and (c), the solid line shows dune altitude along the transect with an arbitrary scale.

example, the profile at point 1 labeled "downwind" in Figure 4. Therefore, on average, the flow behind the dune did not recirculate per se (A. B. Smith et al., 2017), as it would downstream of a backward-facing step. However, as Figure 3 illustrates, the nature of its turbulence, as measured by the ratio u'/u^* was not consistent with a fully developed turbulent boundary layer, but instead adopted a behavior reminiscent of meandering wind, as would be expected if the dune produced a Kármán vortex street in its wake.

In short, the lee of the dune featured a flow that meandered about the mean wind direction, rather than reversed course. At about twice the distance from the base of the avalanche face to the line joining the downstream tips of the barchan horns, the flow eventually returned to the upstream value of u^*/u_r^*, and fluctuation velocities relative to u^* conformed again to the asymptotic value $(2/3)^{1/2}\chi$ in Equation 10.

5. Much Larger Dune

We also conducted measurements on a dune six times larger than that considered in other sections. In this case, our anemometer triads were well within the inertial inner layer of thickness prescribed by Equation 5. They were carried along the longitudinal transect shown in Figure 6 and left at each position for approximately 20 min. Because this very large dune continuously rose until the brink, we referred shear velocities u^* to their counterpart u_r^* that we simultaneously recorded with the fixed upstream anemometer triad on the rough desert floor.

As Figure 6 illustrates, the profile of relative shear velocity u^*/u_r^* evolved qualitatively as it did on the smaller dune (Figure 5). To investigate behavior at the brink, we left the roving triad at the brink for 18 hr. Within that period, we extracted 10 intervals of 20 min during which the wind blew toward a bearing of $153 \pm 9°$, close to the

historic direction of dunes in the field, thus letting us evaluate error bars shown in Figure 5. The measurement hinted that an anomalously high u^*/u_r^* was also present at the brink. Meanwhile, the evolution of aerodynamic roughness was qualitatively similar to what we will discuss in Section 7, including values of $z_0 \ll z_{0_\infty}$ well below those inferred from the pipe data of Nikuradse (1933).

6. Aeolian Transport

To determine wind speeds at which the transported sand flux changes, we correlated signals of our top anemometer of Figure 1b with those of the acoustic probe that Ahmedou et al. (2007) deployed in the field. In the wind tunnel, their calibrations showed that the transported sand mass flow rate $\dot{q}'$ in a unit width of the whole boundary layer is proportional to a power α of the difference between the voltage V produced by the instrument and a residual voltage V_0 in the absence of any impact, $\dot{q}' \propto (V - V_0)^\alpha \times \mathbb{H}(V - V_0)$, where $\mathbb{H}$ is the Heaviside function equal to 1 when its argument is positive, and zero otherwise.

Specifically, we correlated its series of N voltages V_i with the corresponding N speeds u_{3_i}, which the top anemometer of the fixed triad recorded simultaneously on the dune at a sampling frequency of 1 Hz. To that end, we introduced the normalized correlation function

$$f^\pm(v) = \frac{\sum_{i=1}^{N} \mathbb{H}(u_{3_i} - v) \times (V_i - V_0)^\alpha \times \mathbb{H}(V_i - V_0)}{\sum_{i=1}^{N} \mathbb{H}(u_{3_i}) \times (V_i - V_0)^\alpha \times \mathbb{H}(V_i - V_0)}, \tag{11}$$

where the superscripts $\pm$ indicate, respectively, wind speeds at the top anemometer rising ($u_{3_{i+1}} < u_{3_i}$) or falling ($u_{3_{i+1}} > u_{3_i}$) from one data point to the next. With $v = 0$, the cumulative function $f^\pm$ captured all recorded impacts with voltages $V_i > V_0$, and was therefore equal to one. As v grew, because fewer and fewer impacts occurred with $u_{3_i} > v$, $f^\pm$ decreased. Then, its absolute derivative $|\partial f^\pm/\partial v|$ had local peaks at values of wind speeds where impacts suddenly became more abundant.

Three distinct peaks of $|\partial f^\pm/\partial v|$ are evident in Figure 8. As commonly observed at the onset of other gas-solid suspensions such as minimum fluidization (Tsinontides & Jackson, 1993), each peak exhibits hysteresis, whereby it arises at a higher wind speed when the latter is rising. Such behavior is reminiscent of the wind tunnel experiments of Zhu et al. (2019), who noted that incipient aeolian transport is subject to several thresholds.

We also examined our long-term records on the dune and brink to recognize the unmistakable Bagnold transition to aeolian transport that Zhu et al. (2019) identified as their second threshold (Figures 9b–9d). Below this transition, the log-law in Equation 2 applies, so the shear velocity is proportional to the speed u_3 at the top anemometer of altitude z_3,

$$u^* = \frac{\kappa}{\ln(z_3/z_0)} \times u_3 \equiv s_1 \times u_3. \tag{12}$$

Equivalently, the mean aerodynamic roughness $\bar{z}_0$ may be obtained from the slope s_1 on a graph of u^* versus u_3,

$$\ln\left(\frac{\bar{z}_0}{z_{0_\infty}}\right) = \ln\left(\frac{z_3}{z_{0_\infty}}\right) - \frac{\kappa}{s_1}, \tag{13}$$

in which we make diameters and distance dimensionless with Nikuradse's z_{0_∞} on a rough wall (Equation 4), which is the only natural local length scale. An inspection of Equation 12 indicates that the ratio u^*/u_3 is entirely governed by the magnitude of $\ln z_0$ and therefore, as we suggest in Section 7, by fluid friction alone.

Beyond the transition, a two-way momentum coupling arises between the gas and solids interacting with the erodible bed. Once wind speed is sufficient to saturate the flow with transported particles, Bagnold (1941) observed that the log-law of Equation 2 passes through a single focal point (Nakamura & Tsuchiya, 2013) at the altitude z_b and velocity u_b, implying that shear velocity and aerodynamic roughness are bound by the relation

$$u_b = (u^*/\kappa)\ln(z_b/z_0). \tag{14}$$

As Creyssels et al. (2009), Ho et al. (2011), and O'Brien and Neuman (2019) articulated, the denser population of grains below the focal point extracts momentum from the air, as they collide among themselves, while their solid volume fraction establishes a balance between their pelting of the erodible surface and the subsequent "splash" ejection of new grains. In contrast, above the focal point, the increasingly more dilute mixture allows the air to catch up with the wind speed aloft. As a result, the gas velocity profile adapts its shape to pass through the focal point irrespective of wind speed aloft, which is equivalent to adjusting the apparent z_0 as u^* changes.

Another consequence of Equation 14 is that the slope of u^* versus u_3 rises to a higher value s_2 after aeolian transport has begun. Eliminating $\ln z_0$ between Equations 12 and 14,

$$u^* = \frac{\kappa}{\ln(z_3/z_b)} \times (u_3 - u_b) \equiv s_2 \times (u_3 - u_b). \tag{15}$$

Then, the mean aerodynamic roughness now satisfies

$$\ln\left(\frac{\bar{z}_0}{z_{0_\infty}}\right) = \ln\left(\frac{z_3}{z_{0_\infty}}\right) - \kappa\left(\frac{1}{s_2} + \frac{u_b}{u^*}\right). \tag{16}$$

To evaluate the magnitudes u_c^* and $\bar{z}_{0_c}$ of shear velocity and aerodynamic roughness at the critical transport transition, we fit s_2, u_b and the transition speed u_{3_c} to Equations 12 and 15, and substitute the results in Equations 15 and 16. As insets b–d of Figure 9 show, we observe such transition to aeolian transport on the dune and brink, manifested as sharp changes in the graph of $\ln z_0^\dagger$ versus $\ln Re^*$, and also in u^* versus u_3, in agreement with similar wind tunnel observations of Ho et al. (2011) and Zhu et al. (2019). For the triad fixed on the dune, Figure 9f also reveals that this Bagnold transition occurs between the second and third peaks of $|\partial \bar{f}^-/\partial v|$. Similar to what Zhu et al. (2019) reported, this behavior suggests that the first two peaks are precursors to the onset of particle transport, while the third occurs after such transport is initiated.

Inspired by McEwan and Willetts (1993), Jenkins and Valance (2014) used a simple periodic model to capture differences in the transport behavior of rigid and erodible beds, and elucidated the origin of the focal point that Bagnold had observed. Our field measurements reaffirm the existence of this point, and produce a behavior of u^* versus u_3 that agrees remarkably well with the wind tunnel observations of Ho et al. (2011). Such agreement further confirms the validity of our turbulent profiles, despite the minimum redundancy of three anemometers that our field tactics compelled us to adopt.

7. Aerodynamic Roughness

As the Supporting Information shows, historical data for flat beds reveals that aerodynamic roughness plays a unique role in the onset of sediment transport. To bring this to light, we first compare the results of Nikur-adse (1933) for fully developed turbulent flow in rough pipes against research inspired by the work of Shields (1936) for water-based sedimentology, as thoroughly reviewed, for example, by Guo (2020), extended to the density of air first by Bagnold (1941) and to rarefied gases by Andreotti et al. (2021).

In this re-examination, we notice a striking direct proportionality between the threshold Shields number Sh that makes the shear stress $\tau_c = \rho u_c^{*2}$ on a plane at incipient transport of cohesionless, narrowly sorted sediment dimensionless with the weight of particles minus their buoyancy, and the aerodynamic roughness z_0 referenced to its value $z_{0_\infty} = \bar{d}/\varpi$ at large Re^*, once suitably corrected for the ratio of fluid to solid material densities (Pähtz & Duràn, 2023),

$$\text{Sh} \equiv \frac{\tau_c}{(\rho_s - \rho)\, g\, \bar{d}} = \text{Sh}_\infty^* \times \frac{z_0}{z_{0_\infty}} \times \left(\frac{\rho}{\rho_s}\right)^{1/3}, \tag{17}$$

where $\text{Sh}_\infty^* = 0.0660 \pm 0.0053$ at 95% confidence or, equivalently, $\tau_c = \tau_\infty^* \times (\rho_s - \rho)\, g\, z_0\, (\rho/\rho_s)^{1/3}$ with $\tau_\infty^* = 2.28 \pm 0.18$. This simple correlation suggests an interpretation of z_0/d, not as a geometrical parameter, but

rather as controlling the Coulomb-like threshold friction that the turbulent boundary layer must exert on a sediment surface to mobilize its constituent particles. Because Prandtl's mixing length κz in the turbulent core above a plane surface is proportional to the distance z from it (Bradshaw, 1974), Equation 2 implies that κz_0 is a natural scale for this length. It is intriguing that Equation 17 can then be recast as $\text{Sh} = (\tau_\infty^*/\kappa) \times (m_0/m_s)^{1/3}$, where m_0 is the mass of a characteristic fluid eddy of diameter κz_0 and m_s is the mass of a typical particle on the planar surface.

To obtain Equation 17, we integrate Equation 2 across Nikuradse's pipes of radius R_p, relate z_0/R_p to the Darcy friction factor that Nikuradse reported, and recall that his entire data set conforms to a single curve that is equivalent—albeit much simpler—than the Moody (1944) chart (Figure 10b),

$$z_0^\dagger \equiv \frac{z_0}{z_{0_\infty}} = \frac{\exp(-a_{u_0}\,\kappa)}{\text{Re}^*} + 1 - \exp(-a_z\,\text{Re}^*), \tag{18}$$

where $\text{Re}^* \equiv u^* z_{0_\infty}/\nu$ and $z_0^\dagger$ characterize the local turbulence, $a_{u_0} = 5.84 \pm 0.04$ and $a_z = 1.35 \pm 0.03$ (J. Cheng et al., 2022; Christoffersen & Jonsson, 1985; Dade et al., 2001; J. D. Smith, 1975). Then, we note the remarkable resemblance of Equation 18 and available literature correlations for Sh versus Re^* across systems spanning nearly six orders of magnitude in ρ/ρ_s (Andreotti et al., 2021; Jia et al., 2023; Pähtz & Duràn, 2018; Swann et al., 2020). Three regimes naturally arise from Equation 18, namely a low Re^* limit for $\ln \text{Re}^* < (a_{u_2} - \kappa\,a_{u_0})/(1 + a_{u_1})$ where $\ln z_0^\dagger \simeq -a_{u_0}\,\kappa - \ln \text{Re}^*$, an intermediate transition where $\ln z_0^\dagger \simeq -a_{u_2} + a_{u_1} \times \ln \text{Re}^*$, and a rough limit for $\ln \text{Re}^* > a_{u_2}/a_{u_1}$, where $\ln z_0^\dagger \simeq 0$ (straight lines in Figure 10b with $a_{u_1} \simeq 0.234 \pm 0.015$ and $a_{u_2} \simeq 0.184 \pm 0.010$).

Because Equation 18 is independent of the outer scale R_p of Nikuradse's pipes, turbulent fluid mechanics has long posited that Equation 18 should apply to any fully developed turbulent boundary layer, as long as the underlying surface is flat and its bumpiness is invariant. However, it is unclear whether Equations 17 and 18 should hold with wide variations of topography and/or surface bumpiness, or whether the permeable nature of sediment surfaces might also play a role.

As this section articulates, our field data suggests that the local geometrical roughness $z_{0_\infty} = \bar{d}/\varpi$ no longer serves as reference scale for the Shields parameter Sh in Equation 17. Given the long reach of turbulent coherent structures, it appears that such reference is closer to the much larger—and more distant—z_{0_f} from the surrounding desert floor.

Although all velocity profiles conformed to the logarithmic form in Equation 2, the corresponding $\ln z_0$ were more uncertain than those of u^* discussed in Section 3. Unlike u^*, values of $\ln z_0$ drawn from the lowest anemometers did not reside within the regression error bars $\ln z_0 \pm \Delta \ln z_0$ at 80% confidence. As the Supporting Information shows (Louge et al., 2023), for nearly half roving locations on the small dune, $(\ln z_0)_{n=3}$ calculated from three anemometers was higher than its counterpart $(\ln z_0)_{n=2}$ drawn from the lowest two. In this case, we conservatively pushed the size of the lower error bar of $\ln z_0$ down to $(\ln z_0)_{n=2}$, and reported $\ln z_0 \in \left[\ln z_0 - (\ln z_0)_{n=3} + (\ln z_0)_{n=2}, \ln z_0 + \Delta \ln z_0\right]$; conversely, if $(\ln z_0)_{n=3} < (\ln z_0)_{n=2}$, we widened the confidence interval as $\ln z_0 \in \left[\ln z_0 - \Delta \ln z_0, \ln z_0 + (\ln z_0)_{n=2} - (\ln z_0)_{n=3}\right]$.

As Equation 13 indicates, aerodynamic roughness is independent of wind speed below the transport threshold. However, it exhibited greater scatter than the relative shear velocities u^*/u_r^* reported in Section 4. Nonetheless, clear trends emerged. First, in agreement with predictions of Ho et al. (2011), the hard desert floor did not undergo a regime transition in $\ln z_0$ from Equations 13–16, as aeolian transport was negligible between dunes. Here, we found that the nearly constant ratio $s_1 \equiv u^*/u_3$ was greater than at the brink or on the dune, consistent with the much greater $\ln z_{0_f}$ of the rock-covered desert floor. Coincidentally, the data suggested a downward trend of z_{0_f} versus u^* on the desert floor, namely $\ln(u^* z_{0_f}/\nu) = 5.05 \pm 0.38$, which resembled the similar relation for a perfectly smooth wall (Equation 3), but with a much larger constant.

As Figures 9 and 10a illustrate, the magnitude of $\ln z_0/z_{0_\infty}$ at the brink and on the dune proved considerably larger than what Equation 18 predicts. The field data of Sauermann et al. (2003) on a large dune in Brazil (gray rectangle in Figure 10a) confirms this (Because those authors only recorded wind speed with a single anemometer, they inferred u^* by adopting the relatively large invariant value $z_0 = 250$ μm that produced best agreement with the
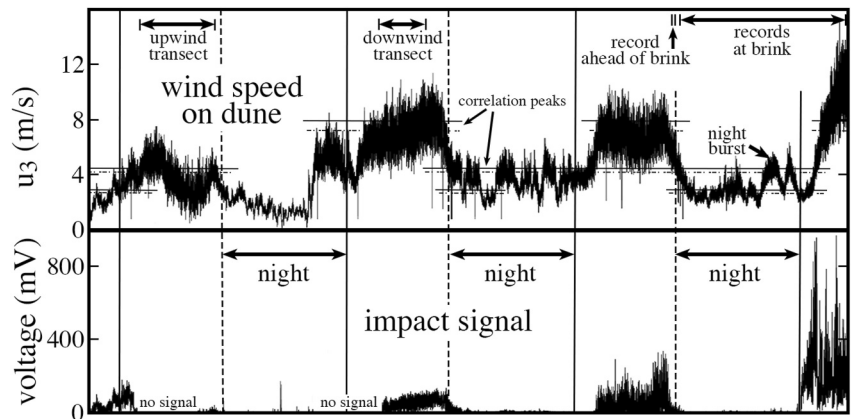
Figure 7. Records of speed at the top anemometer fixed on the dune and the corresponding impact signal (bottom). Sunrises and sunsets are marked by vertical solid and dashed lines, respectively. The first sunrise is on 11 January 2017 and the last on 14 January. Horizontal arrows indicate when specific measurements were conducted, including roving anemometry on the main longitudinal "upwind transect" identified in Figure 1, the corresponding "downwind transect", measurements performed "upstream of brink" (diamonds in Figure 11 upper right), and a much longer period with the roving triad gathering "records at brink" at a 0.92 m distance from the latter. Horizontal lines mark correlation peaks found in Figure 8. Note acoustic signal failures on the first and second day.

Jackson and Hunt (1975) theory applied to the dune cross-section transect prolonged by the wake-enclosing solidified streamline of Kroy et al. (2002)).

Crucially, our data of $\ln z_0/z_{0_\infty}$ was also randomly distributed between Equation 18 and the greater value recorded on the desert floor, particularly at the brink. This observation hinted that upstream coherent structures generated by relatively large stones littering the dune's surroundings were occasionally advected by the flow climbing over it. These wide excursions in z_0 at relatively low speeds (Figure 9f) also suggest an explanation for the apparent contrast in acoustic signal strength between the relatively weaker winds on the first day and stronger ones thereafter (Figure 7). Although the transport threshold is driven by u^* (or equivalently by z_0 as Equation 17 suggests), it is not practical to correlate instantaneous acoustic impact signal with a shear velocity that requires a long averaging period. Therefore, the only feasible correlation involves instantaneous wind speed and acoustic signal (Figure 8). Consequently, because wide excursions in z_0 can change the speed threshold, acoustic signal strengths recorded at the same wind speed can differ between periods of relatively weak winds when z_0 varies widely, and stronger winds when z_0 changes more steadily. Avoiding this apparent contrast is the reason why the correlation of Equation 11 involves Heaviside functions of speed $\mathbb{H}(u_{3_i} - v)$ and $\mathbb{H}(u_{3_i})$.

As aeolian transport began, particles dampened fluctuations in $\ln z_0/z_{0_\infty}$ considerably. This suggested that aerodynamic roughness was now exclusively governed by the local flow, rather than more distant coherent structures inherited from the desert floor. As wind speed and shear velocity grew further, greater particle loadings ultimately led to the Bagnold regime transition, which occurred just below the onset of the third peak of $|\partial f^{\pm}/\partial v|$ in Figure 8.

In the absence of aeolian transport, other transects exhibited wide variations in $\ln z_0/z_{0_\infty}$ that were further at odds with Equation 18 (Figure 10a), most notably on the West side of the small dune, where $\ln(z_0/z_{0_\infty})$ turned sharply negative (Figure 11h). Therefore it is obvious that the flow over these dunes did not behave as Nikuradse's fully developed turbulent boundary layer on a rough pipe wall. Such sharp decrease in $\ln z_0^{\dagger}$ is reminiscent of the experimental observations of Antonia and Luxton (1971), Antonia and Luxton (1972), who noted that the interplay of the inner and outer layers delays the return to turbulent equilibrium when a flat surface undergoes a geometrical transition from rough-to-smooth, which is analogous to our dunes on a
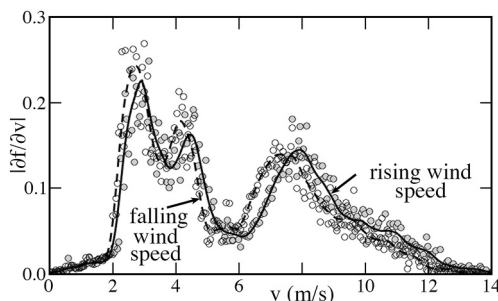
Figure 8. Derivative $|\partial f^{\pm}/\partial v|$ of the function in Equation 11 versus speed v. Peaks of $|\partial f^{-}/\partial v|$ occur at $v = 2.71$, 4.15, and 7.26 m/s with falling wind speeds; peaks of $|\partial f^{+}/\partial v|$ are at $v = 2.90$, 4.47, and 7.94 m/s with rising wind speeds.
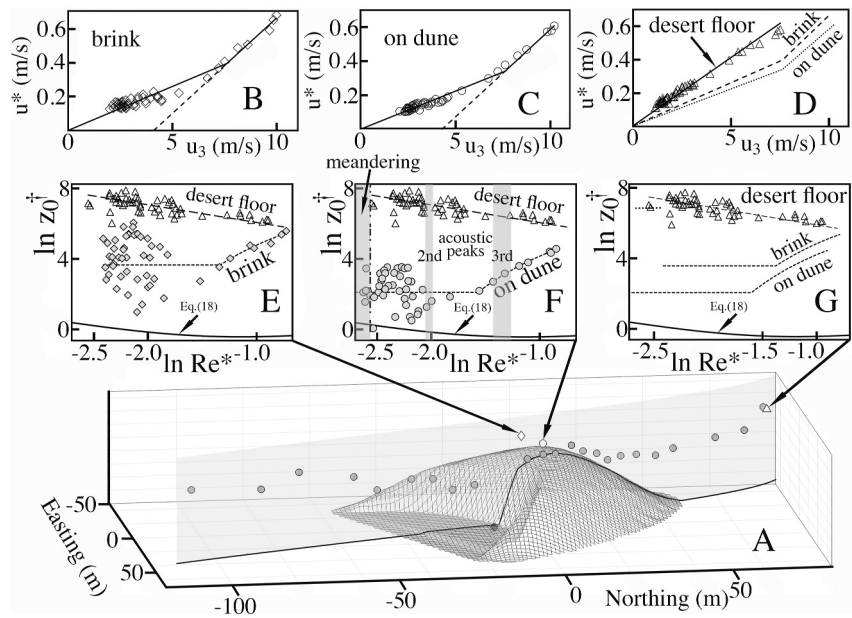
Figure 9. Evolution of shear velocity u^* and $\ln z_0^\dagger$ along the main transect. (a) 3D-sketch showing values of u^*/u_r^* (symbols) along the transect path (solid line), and a dune mesh with exaggerated elevation; the reference u_r^* was recorded simultaneously on the fixed dune triad (circle just West of the transect). Long term records acquired on the windward desert floor (triangles), on the dune (circles) and at the brink (diamonds). (b–d) u^* versus u_3 at the top anemometer at the three locations shown. The solid line is the model of Equations 12 and 15. For the brink (b) and dune data (c), dashed lines prolong the greater slope backward and intersect the u_3-axis at the Bagnold speed u_b. (d) There is no slope change on the hard desert floor, as Ho et al. (2011) predicted; models for brink and dune are superimposed for comparison. (e–g) $\ln z_0^\dagger \equiv \ln(z_0/z_{0_\infty})$ versus $\ln \mathrm{Re}^* \equiv \ln(u^* z_{0_\infty}/\nu)$, where $\bar{d} \simeq 351$ μm is the mean sand grain diameter. In each graph, triangles show values on the desert floor, conforming to $\ln(u^* z_{0_f}/\nu) = 5.05 \pm 0.38$ (dashed line), in good agreement with prior data $\ln(z_{0_f}/z_{0_\infty}) \simeq 6.9$ from Louge et al. (2013) (horizontal dotted line). Dashed lines indicate the model of Equations 13 and 16, and the solid line is Equation 18. (f) $\ln z_0^\dagger$ on the dune (circles); gray areas cover the range of $\ln \mathrm{Re}^*$ for meandering flow, and values between the falling and rising velocities of the second and third peaks of $|\partial f^-/\partial v|$ in Figure 8.

rocky floor, than when it does from smooth-to-rough. In addition, these authors found that the parameter a_u is considerably larger after a rough-to-smooth transition than on a smooth flat surface, reaching a value as high as $a_u \sim 15$, and that κ is also >0.41 in this case. These trends suggest how $\ln z_0^\dagger$ could be smaller than Nikuradse's data.

Conversely, to explain why much larger values of $\ln z_0^\dagger$ are possible, we note that aerodynamic roughness on the dune may be corrupted by its much larger value on the desert floor, as one gradually evolves into the other (Abkar & Porté-Agel, 2012). Our records of incipient transport in Figure 9 offer further insight on the decisive role that the bumpier upstream desert floor plays. As insets (c) and (d) of Figure 10 show, Shields friction coefficients on the dune and its brink are at once *higher* than literature values for $\mathrm{Sh}^* \equiv \mathrm{Sh}(\rho_s/\rho)^{1/3}$ versus Re^*, and *lower* than the expression of Equation 17 for Sh^* versus z_0/z_{0_∞}. Therefore it is clear that our threshold data do not conform to established expressions of Shields friction versus local Reynolds number. However, if we adopt a larger reference z_{0_r} for aerodynamic roughness in the range $z_{0_\infty} < z_{0_r} < z_{0_f}$ where it is expected, the data can be brought into compliance with Equation 17, see dashed lines in Figure 10d. Overall, this suggests that the higher, distant upstream bumpiness affects Shields friction in ways that traditional sedimentology correlations with local Re^* do not capture.

8. Model

We now examine whether the theory of Jackson and Hunt (1975) and Hunt et al. (1988) captures the evolution of the relative shear velocity u^*/u_r^* that we measured on all longitudinal and lateral transects of the smaller dune. Weng et al. (1991) and Kroy et al. (2002) wrote the corresponding two-dimensional Fourier transforms of shear
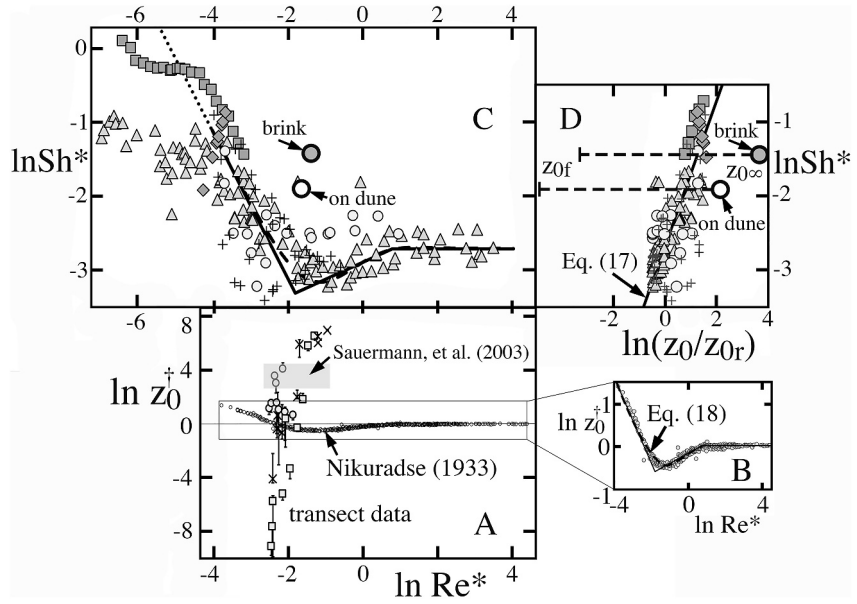
Figure 10. Aerodynamic roughness and density-corrected Shields number $\mathrm{Sh}^* \equiv \mathrm{Sh} \times (\rho_s/\rho)^{1/3}$. (a) $\ln z_0^\dagger$ versus $\ln \mathrm{Re}^*$ for upwind transects without aeolian transport revealing a wide discrepancy with Nikuradse data (small circles). Gray circles are transects labeled "along the dune" in Figure 11, excluding relatively low wind speeds (open circles in Figure 5) or the brink; squares are transects "along the West side"; crosses are for the large dune of Figure 6. Confidence intervals for $\ln z_0^\dagger$ are drawn for all symbols, yet sometimes too small to be visible. The gray rectangle is the likely data range of Sauermann et al. (2003), which we inferred from their reported $u^* \simeq 0.36$ m/s, $z_0 = 250$ μm and particle size $100 < d < 600$ μm (Jimenez et al., 1999). (b) Close-up of Nikuradse data. The solid curve and dashed straight lines are, respectively, Equation 18 and its approximation in three regimes. (c) $\ln \mathrm{Sh}^*$ versus $\ln \mathrm{Re}^*$ from Guo (2020) (triangles), Pähtz and Duràn (2018) (circles), Swann et al. (2020) (diamonds), Andreotti et al. (2021) (squares), and simulations of Pähtz and Duràn (2023) (pluses). Solid curve and dashed lines are obtained by adopting Equation 18 to convert $\ln \mathrm{Re}^*$ to $\ln z_0^\dagger$, and Equation 17 to transform $\ln z_0^\dagger$ into $\ln \mathrm{Sh}^*$. For $\ln \mathrm{Re}^* < -4$, the correlation no longer applies as the flow is not fully turbulent (dotted line), but rarefied conditions (squares) still conform. Large circles are data for $\ln \mathrm{Sh}^*$ versus $\ln \mathrm{Re}_c^* = \ln(u_c^* z_{0_\infty}/\nu)$ at the brink and on the triad fixed on the dune. (d) $\ln \mathrm{Sh}^*$ versus $\ln(z_0/z_{0_r})$ for literature data (symbols in inset c) and the corresponding fit of Equation 17 (line). Large circles are brink and dune data assuming $z_{0_r} = z_{0_\infty}$; the dashed line spans the range $z_{0_\infty} < z_{0_r} < z_{0_f}$ where we expect the reference aerodynamic roughness z_{0_r} to reside.

stress excursions $\hat{\tau}_x$ and $\hat{\tau}_y$, respectively along the wind and across its transverse direction, from the mean value ρu_∞^{*2} far away on the surrounding plane, due to the presence of a bedform of elevation $h(x, y)$ above the horizontal,

$$
\begin{aligned}
\frac{\overline{\hat{\tau}_x}}{\rho u_\infty^{*2}} &= \frac{A k_x^2 + \iota B k_x |k_x|}{\sqrt{k_x^2 + k_y^2}} \times \overline{h} \\
\frac{\overline{\hat{\tau}_y}}{\rho u_\infty^{*2}} &= \frac{k_x \times k_y}{\sqrt{k_x^2 + k_y^2}} \times \overline{h},
\end{aligned}
\tag{19}
$$

where $k_x = 2\pi/\lambda_x$ and $k_y = 2\pi/\lambda_y$ are respective wavenumbers along and across the wind, λ_x and λ_y are the corresponding wavelengths, and the overbar denotes the Fourier transform. As mentioned earlier, Fourrière et al. (2010) calculated A and B in terms of $\eta_0 \equiv 2\pi z_0/\lambda$ and $R \equiv -\ln(z_0/\lambda) > 0$.

Meanwhile, to address the meteorological problem of wind transitioning from the ocean surface to a flat landform, Walmsley et al. (1986) considered variations in aerodynamic roughness on a horizontal plane without topographical evolution. For a roughness satisfying $\ln z_0 = \ln z_{0_f} + a_g \times G(x, y)$, where G is a dimensionless function, a_g is an amplitude of its variations, and $\ln z_{0_f}$ is roughness around the bedform, they obtained the Fourier transform of stress excursions

$$\overline{\frac{\hat{\tau}_{z_0}}{\rho u_\infty^{*2}}} = \frac{a_g \times \overline{G}}{K_0\left(2\sqrt{\imath\, z_{0_f}\, k_x}\right)},\tag{20}$$

where K_0 is the modified Bessel function of the second kind and order zero.

To predict the shear stress on the entire dune surface, we first identify the dune outline on hard ground from theodolite measurements, least-squares-fit the plane on which it stands, and slightly tilt the entire dune so this outline becomes horizontal (Figure 1). For each position of the roving anemometer triad, we then rotate the resulting three-dimensional surface to align it with the time-averaged wind direction during the measurement period. To avoid aliasing the Fourier-transformed height $\bar{h}$, we pad the (x,y) domain where the dune resides with at least one identical area of vanishing altitude on all sides.

Recently, Jia et al. (2023) extended the Jackson and Hunt framework to variations of $\ln z0$ with topography. Unfortunately, in our case, because such variations are superimposed upon drastic changes of geometrical roughness between the dune and its surroundings, we crudely estimate the contribution $\hat{\tau}_{z_0}$ of roughness evolution to the shear stress in Equation 20 by fitting our measurements of $\ln z_0$ to the empirical function

$$G \simeq \frac{1}{(2g_1 + g_2)} \times \left[(4g_1 + 3g_2)\left(\frac{h}{h_{\max}}\right)^2 - 2g_2\left(\frac{h}{h_{\max}}\right)^3 - 2g_1\left(\frac{h}{h_{\max}}\right)^4 \right],\tag{21}$$

where $a_g = -(g_1 + g_2/2)$, $g_1 = -86 \pm 20$, $g_2 = 180 \pm 40$.

Finally, we identify the dimensionless shear stress excursions as the real part of the inverse transforms in Equations 19 and 20, calculate the vector $\boldsymbol{\tau}(x,y) = \rho u_\infty^{*2}\, \hat{\mathbf{x}} + \hat{\tau}$, where all contributions to stress deviations are combined linearly as $\hat{\tau} = (\hat{\tau}_x + \hat{\tau}_{z_0})\, \hat{\mathbf{x}} + \hat{\tau}_y\, \hat{\mathbf{y}}$, and derive $\rho u^{*2} \equiv \|\boldsymbol{\tau}\|$. Figure 11 compares measurements and predictions of Equation 19 with or without the contribution of Equation 20. Although the linear theory of Equation 19 should not apply to sudden or steep variations of topography, it predicts the correct trends on the main longitudinal transect (solid line, inset b), namely an initial dip in u^*/u_r^* as one approaches the windward face, followed by a rise toward the crest, a sharp peak at the brink, a reversal at the foot of the slip face, and a gradual return to the upstream u_∞^*/u_r^* behind the dune. In general, we find that the contribution of $\hat{\tau}_y$ is relatively small. Near the brinkline (inset f), we plot predictions on a parallel path at the distance of 0.92 m where an anomalous peak arose (open diamond). As expected, measurements at greater separation from the brinkline exhibit lower values of u^*/u_r^*.

Nonetheless, Equation 19 typically overpredicts u^*/u_r^*, and it does not capture transverse transects well (inset c). In addition, Equation 19 alone fails to reproduce a substantial dip in u^*/u_r^* on the off-center longitudinal transect (inset e). However, this feature is qualitatively captured by adding the contribution of Equation 20. Similarly, the dotted line in inset (b) suggests that variations in $\ln z_0$ are responsible for the initial decrease in u^*/u_r^* along the main transect.

In short, to model surface shear stress on a dune with vastly different geometrical roughness than its surrounding, it is essential to know how topography and aerodynamic roughness both evolve. However, while topography is straightforward to establish, aerodynamic roughness cannot yet be predicted a priori without measuring turbulent velocity profiles in the field.

9. Role of Dune Skewness

Although the theory exaggerates predictions of u^*/u_r^*, we use it on artificial dune profiles of invariant roughness to suggest how a local peak of shear velocity arises near the brink. Kroy et al. (2002) conducted such exercise on Gaussian-shaped bedforms, occasionally truncated to feature an avalanche face. Recognizing that the linear theory was not meant to handle a sharp discontinuity in slope, they extrapolated the dune surface beyond the brink with the upper streamline of a separation "bubble" bounding its wake, which they approximated as a cubic profile with distance. To find the downwind landing position and the four coefficients of this cubic, they imposed a continuous altitude and slope at the brink, vanishing altitude and slope at the landing, and they prescribed that the
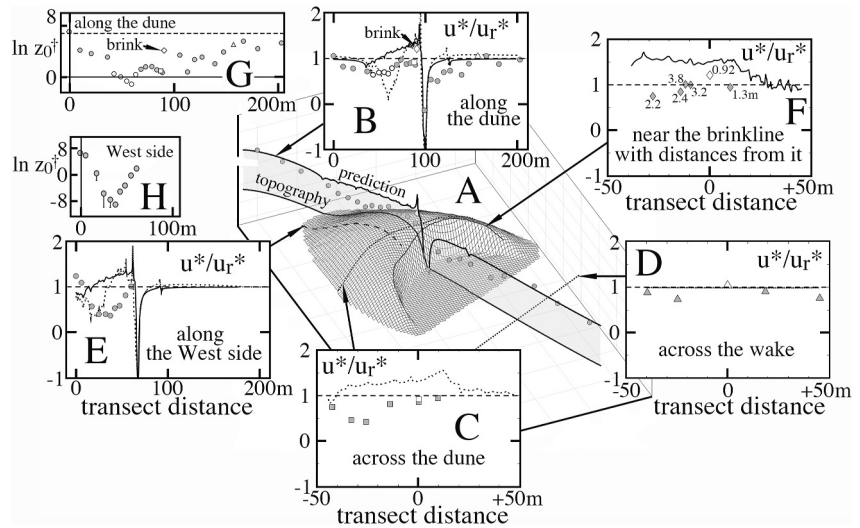
Figure 11. Measured transects of u^*/u_r^* versus distance x and predictions of Equation 19. (a) dune topography with exaggerated altitude and superimposed transects (thick solid line: longitudinal transect in Figure 5; dashed line: "along the West side"; dotted line: "across the dune" or "across the wake"; thin line along the brink). The solid line marked "prediction" is Equation 19 and also appears in inset (b) "along the dune" with identical symbols for u^*/u_r^* (filled circles for longitudinal transects; open diamond for the anomalous value at the brink, see also Figure 9). (b–f) Lines are predictions of Equation 19 alone for an average wind direction among measurements in each transect; open squares (c) and triangles (d) mark intersections of two transects nearly orthogonal to (b); circles are "along the dune" (b), squares "across the dune" (c), triangles "across the wake" (d), or its "West side" (e); diamonds are "near the brinkline" (f) with corresponding distances from it. Like Figure 5, open circles mark measurements at low wind speeds. In panels (b) and (e), solid lines are Equation 19 alone, while dotted lines add the contribution of Equation 20 with $a_g = -2.2$ and $\ln(z_{0_f}/z_{0_\infty}) = 6.2$ for (b) and $\ln(z_{0_f}/z_{0_\infty}) = 4.9$ for (e). (g) Transect of $\ln z_0^\dagger$ along the dune while $u_r^* = 0.14 \pm 0.03$ m/s for $0 < x < 88$ m, later rising to $u_r^* = 0.35 \pm 0.03$ m/s for $106 < x < 203$ m. (h) Surprisingly, $\ln z_0^\dagger$, shown here with its confidence intervals, turned sharply negative along the West side, while $u_r^* = 0.31 \pm 0.02$ m/s varied little.

inclination of the streamline in between have its steepest inclination equal to 14°. Here, we revisit this exercise to gauge whether the theory, when applied to bedforms with sharper variations, may yet foreshadow the existence of the anomalous peak of u^*/u_∞^* that our field tests revealed.

Figure 12 illustrate these calculations, which for simplicity we carry out without variations in $\ln z_0$. In inset a, we first consider an artificial three-dimensional dune with geometry prescribed by Sauermann et al. (2000). As Kroy et al. (2002) intended, fitting a separation bubble (dotted line) hardly induces a peak in the profile of u^*/u_∞^* on the centerline transect. However, forsaking this artificial bubble yields considerable excursions in this ratio, including a sharp rise at the brink and a depression at the toe (solid line). Coincidentally, this line also features a sharp reversal in $u^*/u_\infty^* < 0$ just behind the lee, although it exaggerates what was observed in Figure 4. Meanwhile, a Gaussian profile with similar profile standard deviation confirms that the maximum u^*/u_∞^* on such smooth bedform arises ahead of the crest (dashed line).

In insets b and c, we note that a sharp peak in u^*/u_∞^* can also arise without an abrupt discontinuity in slope. In the spirit of Kroy et al. (2002), we show this by constructing artificial bedforms of height h_0 that are shaped as a symmetric Gaussian in the direction y perpendicular to the wind, but that are asymmetric down its bearing of coordinate x. The asymmetry along x is achieved by patching two half-Gaussians of different standard deviations s_x^+ for $x > 0$ and s_x^- for $x < 0$,

$$h = h_0 \exp\left[\frac{1}{2}\left(\frac{y}{s_y}\right)^2\right]\left\{\mathbb{H}(x)\exp\left[\frac{1}{2}\left(\frac{x}{s_x^+}\right)^2\right] + \mathbb{H}(-x)\exp\left[\frac{1}{2}\left(\frac{x}{s_x^-}\right)^2\right]\right\}, \tag{22}$$

where $\mathbb{H}(x)$ is the Heaviside function, thus making the profile continuous in elevation and slope on its crest at $x = 0$, albeit discontinuous in the second derivative. (Such profile resembles the larger dune in Figure 6, which
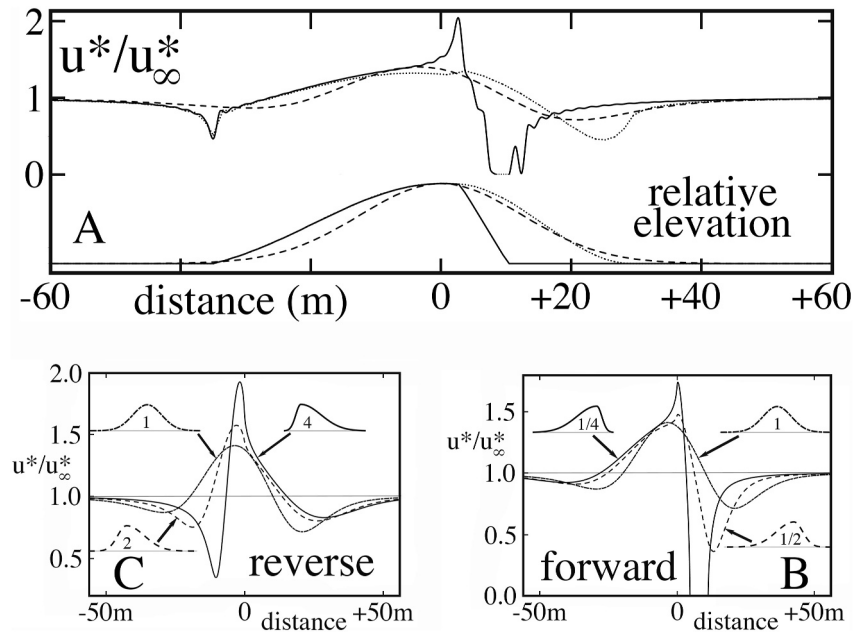
Figure 12. Shear velocity u^* relative to its upwind value u^*_∞ and dune elevation h relative to its crest height h_0 along the central symmetry transect in the prevailing wind direction on artificial three-dimensional dunes, predicted by Equation 19. (a) Solid lines: dune shaped as described by Sauermann et al. (2000) with identical $h_0 \simeq 4.5$ m as its real counterpart in Figure 1. Dotted lines are for the same dune artificially prolonged with a separation bubble (Kroy et al., 2002). Dashed lines are for a bedform shaped as a symmetric Gaussian with standard deviations $s_x^+ = s_x^- \simeq 12.5$ m and $s_y \simeq 12.2$ m of the dashed bedform profile. (b, c) Profiles of u^*/u^*_∞ on artificial bedforms conforming to Equation 22 with central transects shown in three insets labeled with their coefficient $\beta \equiv s_x^+/s_x^-$. (b) Profile resembling a barchan with steeper downwind face. Solid, dashed and dotted line have, respectively, $\beta = 1/4$, $1/2$ and 1 (skewness $\tilde{\mu}_3 \simeq -0.8$, -0.5 and 0). (c) A higher peak of u^*/u^*_∞ arises as wind reverses direction ($\beta = 4$, 2, and 1 as shown, or $\tilde{\mu}_3 \simeq +0.8$, $+0.5$, and 0, respectively). $u^* < 0$ is truncated for clarity.

reaches its highest elevation at the brink). We set different ratios $\beta \equiv s_x^+/s_x^-$ of the artificial bedform, while keeping the sum $\bar{s}_x^2 \equiv \left[\left(s_x^+\right)^2 + \left(s_x^-\right)^2\right]/2$ constant. To characterize the topographical profiles of Equation 22, we introduce their skewness

$$\tilde{\mu}_3 = \int_\infty^{+\infty} \left(\frac{x - \mu_d}{\sigma_d}\right)^3 h^* \mathrm{d}x, \tag{23}$$

where $\mu_d \equiv \int_\infty^{+\infty} x h^* \mathrm{d}x$, $\sigma_d \equiv \int_\infty^{+\infty} \left(x - \mu_d\right)^2 h^* \mathrm{d}x$, and $h^* = h/\int_\infty^{+\infty} h \, \mathrm{d}x$ is normalized. However, it is more intuitive to quote the ratio β of the right and left standard deviations s_x^+ and s_x^-, which is related to $\tilde{\mu}_3$ by integrating Equation 22,

$$\tilde{\mu}_3 = \sqrt{2}(1 - \beta)\frac{\pi - 4(1 - \beta)^2 + \pi(\beta - 3)\beta}{\left[\pi - 2(1 - \beta)^2 + \pi(\beta - 1)\beta\right]^{3/2}}. \tag{24}$$

We find that a backward flow (inset c) yields stronger peaks of u^*/u^*_∞ than its forward counterpart on the gentler slope (inset b), consistent with common observations of more intense erosion at the brink of a barchan when wind reverses direction. Crucially, as both insets show, the peak of u^*/u^*_∞ near $x = 0$ grows as magnitude of the profile skewness $\tilde{\mu}_3$ increases along the wind transect. Therefore, despite its flaws illustrated in Figure 11, the theory of Jackson and Hunt (1975) suggests that skewness of the dune profile is the principal cause of the anomalous peak of shear stress that our field measurements revealed at the brink.
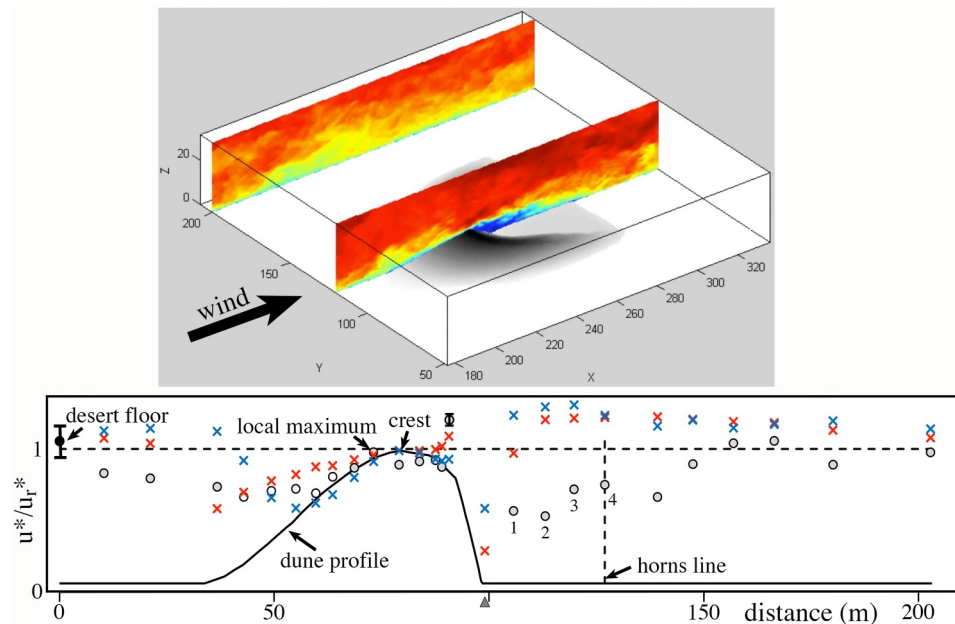
10. Large-Eddy Simulations

In the absence of aeolian transport, Section 7 implied that, despite its universal character for rough walls, Equation 18 is inappropriate when topography and/or large, sudden variations in surface bumpiness exist. In this context, we investigated whether LES, which generally assume $\ln z_0$ at the boundary, address the challenge of wide variations of aerodynamic roughness on the surface.

Turbulent flows over large bedforms are challenging to compute with fidelity (Smyth, 2016). Most efforts have focused on improving the size and resolution of numerical simulations by scaling-up the domain of LES (Hardy et al., 2021; Jin et al., 2021; Liu et al., 2019; Omidyeganeh & Piomelli, 2013; Sun & Zheng, 2023; Zheng et al., 2020), RANS (Jin et al., 2021; Lane et al., 2004; Lefebvre et al., 2014; Michelsen et al., 2015; A. B. Smith et al., 2017), or algorithms coupling morphodynamics with a fluid mechanics solver such as Lattice methods (Baumgarten et al., 2021; Lü et al., 2018; Narteau et al., 2009; Q. Zhang et al., 2022), LES or RANS (Sotiropoulos & Khosronejad, 2016), or ad-hoc models of erosion and deposition (Xiao et al., 2023).

In all such techniques, boundary conditions for shear stress and aerodynamic roughness play a crucial role. To gauge their importance, we simulated the turbulent flow over the dune using the large-eddy simulation code WiRE-LES developed at EPFL. To avoid time-consuming computation, LES spatially filters and solves the Navier-Stokes equations, explicitly resolving large turbulent motion while lumping net momentum contributions of small eddies in a subgrid scale (SGS) model. In this way, LES captures much larger flows than direct numerical simulations that employ a grid discretization smaller than all relevant scales in the turbulent energy cascade. To handle flows over long bedforms, our own WiRE-LES combines a spectral method of high-order accuracy in the horizontal directions with finite-difference discretization along the vertical elevation for efficient implementation of wall models (Fang et al., 2018). Using a terrain-following coordinate transformation (Fang & Porté-Agel, 2016), we extend this numerical strategy to topographies with low to moderate slopes, which are typical of desert dunes. Meanwhile, to parameterize unresolved stresses, we adopt the Lagrangian scale-dependent dynamic SGS model of Stoll and Porté-Agel (2006), which does not require parametric tuning and readily applies to complex terrain. Fang and Porté-Agel (2016) validated this approach against wind tunnel data.

To direct the flow through a single inlet and outlet, we rotated the simulation domain to align the x-axis with wind direction. We placed the barycenter of the dune outline at the center of the (x, y) plane, discretized the 512, 128, and 64 m domain in a regular grid of resolution of $\Delta x = \Delta y = 1$ m and $\Delta z \simeq 0.25$ m along the x-, y- and z-directions, respectively. The spectral method automatically applied periodic boundary conditions in the horizontal directions. We specified the upper boundary condition as stress-free. Because dimensions of the domain in the y- and z-directions were much larger than the dune size, those boundary conditions did not affect the flow in the dune vicinity significantly. We imposed turbulent inflow boundary conditions at the inlet using the buffer-zone technique, which conducts a precursor simulation without the dune and drives the flow with a constant mean pressure gradient along the x-direction that matches the velocity profile above the surface to that recorded at the reference anemometer triad.

Crucially, we evaluated the surface shear velocity from Equation 2, which relates the instantaneous velocity in the first grid cell to the assumed $\ln z_0$, ignoring the phase lead of shear stress over topographical variations that is modeled in Equation 19. Figure 13 compares LES predictions of u^*/u_r^* time-averaged over 300 s and data on the main longitudinal transect for two distinct prescriptions of $\ln z_0$. In the first, we adopted for the entire domain the uniform value of $\ln(z_0/z_{0_\infty}) = 3.4$ that is representative of data recorded on the dune (red crosses in Figure 13). As expected, u^* was mismatched ahead of dune, but rejoined measured data on the upstream slope. Although the simulation hinted at the existence of the peak u^* at the brink, it did not capture the local maximum ahead of the crest, perhaps because it did not resolve the inertial inner layer of thickness $\ell \sim \Delta z$ that is central to the Jackson and Hunt (1975) theory. Downstream, the simulation overpredicted u^* and returned to far-field conditions farther than measurements. By analogy with flows near the trailing edge of an airfoil (Dahlström & Davidson, 2003), it is possible that the relatively coarse spatial resolution around the sharp discontinuity at the brink may be responsible for this. To gauge the role of an evolving $\ln z_0$, we also conducted another LES with values of $\ln z_0$ correlated with altitude using Equation 21 (blue crosses in Figure 13). Because this simulation barely recorded the rise of u^* at the brink, this exercise confirmed the important role that $\ln z_0$ plays, but underscored challenges involved in predicting it.

Figure 13. Comparison of field data on the longitudinal transect of u^*/u_r^* of Figure 5 (circles) with Large-eddy-simulations predictions at same location on an identical topography. Red crosses: fixed roughness $\ln(z_0/z_{0_\infty}) = 3.4$; blue crosses: roughness correlated with relative altitude, $\ln z_0 = \ln z_{0_f} + a_g \times G$ from Equation 21 and $\ln(z_{0_f}/z_{0_\infty}) = 6.9$. Top: a snapshot of local streamwise wind velocity (deepest blue: -1.8 m/s and red: $+9.9$ m/s) at fixed roughness. Other symbols, see Figure 5.

11. Conclusions

Deploying triads of two-dimensional ultrasonic anemometers with minimum redundancy, we conducted field experiments to evaluate the evolution of turbulent shear velocity u^* and the log of aerodynamic roughness $\ln z_0$ on two large isolated crescent-shaped barchan sand dunes surrounded by a stone-covered, nearly horizontal desert floor. On a central transect along the prevailing wind direction, u^* first decreased, then climbed over the dune, with a local maximum ahead of its crest. A sharper peak also arose at the brink just ahead of the downwind avalanche face. Although such peak is likely to raise the local sand flux cast over the avalanche face, effects of this anomaly on aeolian erosion at the brink require more research.

Despite its linear character, the theory of Jackson and Hunt (1975) for flows over low hills captured—albeit exaggerated—these trends for u^*, and suggested that dune skewness is responsible for the sharper peak. The model of Walmsley et al. (1986) further implied that observed variations in $\ln z_0$ could qualitatively predict reductions of u^* on the upwind face and on the off-center transect to the West of the dune.

The mean flow did not recirculate on the lee side, except very close to the avalanche base, but instead it maintained a log profile with velocity fluctuations meandering from side to side about the wind direction.

During period of aeolian sand transport, correlations of an acoustic measurement of transported sand flux with wind strength revealed three consecutive peaks preceding distinct behavior of u^* and $\ln z_0$. At speeds higher than the third peak, u^* rose more steeply with wind speed, consistent with the existence of a focal point in the log profile of wind velocity, which Bagnold (1941) had identified.

Our data further cautioned against assuming that aerodynamic roughness is invariant. Having recorded wide excursions in $\ln z_0$ on and around the dune, we showed conclusively that the behavior of $\ln z_0$ versus u^* is sharply at odds with the universal Equation 18 inferred from the experiments of Nikuradse (1933) with fully developed turbulent boundary layers on rough pipe walls.

As we noted by comparing Nikuradse's data to literature on the Shields (1936) threshold, aerodynamic roughness appears to govern the Shields parameter that makes shear stress on a plane at incipient aeolian transport dimensionless. As a result, its evolution should not be assumed but recorded in the field or modeled, perhaps by combining the theories of Jackson and Hunt (1975), Walmsley et al. (1986), and Jia et al. (2023).

In addition, our data for the Shields parameter versus local shear Reynolds number at the brink differed widely from that on the dune, while neither conformed to density-corrected sedimentology correlations for narrowly sorted, cohesionless grains. This suggested that other effects, such as topography, upstream turbulence, or permeability may play an important role.

In general, we illustrated the importance of prescribing proper boundary conditions in models of fluid flow over field-size bedforms. Despite their remarkable ability to capture most flow features, numerical simulations face two main challenges. First, if they do not resolve the relatively thin inertial inner layer, simulations cannot capture the lead of peak shear stress ahead of the peak topography, and thus they might miss the anomalous rise of u^* at the brink. Such limitation might be rectified without demanding an excessively fine resolution by imposing a boundary condition that evolves according to the Jackson and Hunt (1975) model. Second, simulations often prescribe ln z_0, rather than evaluate it over the entire flow field. We have shown that this practice is arbitrary, particularly if a bumpier surface encloses the bedform.

Because turbulence is driven by fluid inertia, flows of Newtonian fluids with different densities share the same kinematic behavior, as long as fluid properties are constant and the pressure gradient in the Navier-Stokes equations is either negligible or compensated by gravity. Therefore, turbulent boundary layers in water and air are qualitatively similar in the absence of sediment transport. Nonetheless, the fundamental reason for the observed density dependence of Equation 17 with a flat sediment bed remains an open problem. Then, although we conducted measurements in a desert, the challenges that they exposed should arise in other systems, such as submarine or fluvial sand dunes, where bedforms also inherit turbulent vortices from their surroundings.

Data Availability Statement

Supporting Data and its reduction are available on the Cornell University eCommons Repository at Louge et al. (2023). Uncertainty analysis of the anemometry is available at Louge et al. (2024).

References

Abdul-Majid, S., Graw, M. F., Chatziefthimiou, A. D., Nguyen, H., Richer, R., Louge, M., et al. (2016). Microbial characterization of Qatari barchan sand dunes. *PLoS One*, *11*(9), e0161836. https://doi.org/10.1371/journal.pone.0161836

Abkar, M., & Porté-Agel, F. (2012). A new boundary condition for large-eddy simulation of boundary-layer flow over surface roughness transitions. *Journal of Turbulence*, *13*, N23. https://doi.org/10.1080/14685248.2012.695077

Ahmedou, D. O., Mahfoudh, A. O., Dupont, P., Moctar, A. O. E., Valance, A., & Rasmussen, K. R. (2007). Barchan dune mobility in Mauritania related to dune and interdune sand fluxes. *Journal of Geophysical Research*, *112*(F2), F02016. https://doi.org/10.1029/2006JF000500

Allen, J. R. L. (1970). The avalanching of granular solids on dune and similar slopes. *The Journal of Geology*, *78*(3), 326–351. https://doi.org/10.1086/627520

Andreotti, B., Claudin, P., & Douady, S. (2002). Selection of dune shapes and velocities. Part 1: Dynamics of sand, wind and barchans. *European Physical Journal B: Condensed Matter and Complex Systems*, *28*(3), 321–339. https://doi.org/10.1140/epjb/e2002-00236-4

Andreotti, B., Claudin, P., Iversen, J. J., Merrison, J. P., & Rasmussen, K. R. (2021). A lower-than-expected saltation threshold at Martian pressure and below. *Proceedings of the National Academy of Sciences*, *118*(5), e2012386118. https://doi.org/10.1073/pnas.2012386118

Anfossi, D., Öttl, D., Degrazia, G., & Goulart, L. (2005). An analysis of sonic anemometer observations in low wind speed conditions. *Boundary-Layer Meteorology*, *114*(1), 179–203. https://doi.org/10.1007/s10546-004-1984-4

Antonia, R., & Luxton, R. E. (1971). The response of a turbulent boundary layer to a step change in surface roughness. Part 1. Smooth to rough. *Journal of Fluid Mechanics*, *48*(4), 721–761. https://doi.org/10.1017/S0022112071001824

Antonia, R., & Luxton, R. E. (1972). The response of a turbulent boundary layer to a step change in surface roughness. Part 2. Rough-to-smooth. *Journal of Fluid Mechanics*, *53*(4), 737–757. https://doi.org/10.1017/S002211207200045X

Babinsky, E., & Sojka, P. E. (2002). Modeling drop size distributions. *Progress in Energy and Combustion Science*, *28*(4), 303–329. https://doi.org/10.1016/S0360-1285(02)00004-7

Bagnold, R. A. (1941). *The physics of blown sand and desert dunes*. Chapman and Hall. https://doi.org/10.1007/978-94-009-5682-7

Baumgarten, A. S., Couchman, B. L., & Kamrin, K. (2021). A coupled finite volume and material point method for two-phase simulation of liquid-sediment and gas-sediment flows. *Computer Methods in Applied Mechanics and Engineering*, *384*, 113940. https://doi.org/10.1016/j.cma.2021.113940

Bradshaw, P. (1974). Possible origin of Prandtl's mixing-length theory. *Nature*, *249*(5453), 135–136. https://doi.org/10.1038/249135b0

Charru, F., Andreotti, B., & Claudin, P. (2013). Sand ripples and dunes. *Annual Review of Fluid Mechanics*, *45*(1), 469–493. https://doi.org/10.1146/annurev-fluid-011212-140806

Charru, F., & Franklin, E. M. (2012). Subaqueous barchan dunes in turbulent shear flow. Part 2. Fluid flow. *Journal of Fluid Mechanics*, *694*, 131–154. https://doi.org/10.1017/jfm.2011.528

Chen, J., Zhang, D., Yang, X., Lehmkuhl, F., & Jiang, W. (2022). The effects of seasonal wind regimes on the evolution of reversing barchanoid dunes. *Journal of Geophysical Research: Earth Surface*, *127*(2), e2021JF006489. https://doi.org/10.1029/2021JF006489

Cheng, N. S., Xu, P., Lu, Y., & Wei, M. (2022). Validation of Bagnold's approximation of critical near-bed flow velocity for incipient sediment motion as particle settling velocity. *Journal of Hydraulic Engineering*, *148*(10), 06022012. https://doi.org/10.1061/(ASCE)HY.1943-7900.0002012

Christoffersen, J. B., & Jonsson, I. G. (1985). Bed friction and dissipation in a combined current and wave motion. *Ocean Engineering*, *12*(5), 387–423. https://doi.org/10.1016/0029-8018(85)90002-2

Claudin, P., Wiggs, G. F. S., & Andreotti, B. (2013). Field evidence for the upwind velocity shift at the crest of low dunes. *Boundary-Layer Meteorology*, *148*(1), 195–206. https://doi.org/10.1007/s10546-013-9804-3

Creyssels, M., Dupont, P., El-Moctar, A. O., Valance, A., Cantat, I., Jenkins, J. T., et al. (2009). Saltating particles in a turbulent boundary layer: Experiment and theory. *Journal of Fluid Mechanics*, *625*, 47–74. https://doi.org/10.1017/S0022112008005491

Dade, W. B., Hogg, A. J., & Boudreau, B. P. (2001). Physics of flow above the sediment-water interface. In B. P. Boudreau & B. B. Jørgensen (Eds.), *The benthic boundary layer* (pp. 4–43). Oxford University Press.

Dahlström, S., & Davidson, L. (2003). Large Eddy Simulation applied to a high-Reynolds flow around an airfoil close to stall (No. 776). In *41st aerospace sciences meeting and exhibit, Reno, NV*. https://doi.org/10.2514/6.2003-776

D'Ippolito, A., Calomino, F., Alfonsi, G., & Lauria, A. (2021). Flow resistance in open channel due to vegetation at reach scale: A review. *Water*, *116*(2), 1–27. https://doi.org/10.3390/w13020116

Durán, O., Claudin, P., & Andreotti, B. (2011). On aeolian transport: Grain-scale interactions, dynamical mechanisms and scaling laws. *Aeolian Research*, *3*, 243–270. https://doi.org/10.1016/j.aeolia.2011.07.006

Durán, O., Parteli, E. J., & Herrmann, H. J. (2010). A continuous model for sand dunes: Review, new developments and application to barchan dunes and barchan dune fields. *Earth Surface Processes and Landforms*, *35*(13), 1591–1600. https://doi.org/10.1002/esp.2070

Fang, J., Peringer, A., Stupariu, M., Pătru-Stupariu, I., Buttler, A., Golay, F., & Porté-Agel, F. (2018). Shifts in wind energy potential following land-use driven vegetation dynamics in complex terrain. *Science of the Total Environment*, *639*, 374–384. https://doi.org/10.1016/j.scitotenv.2018.05.083

Fang, J., & Porté-Agel, F. (2016). Intercomparison of terrain-following coordinate transformation and immersed boundary methods in large-eddy simulation of wind fields over complex terrain. *Journal of Physics: Conference Series*, *753*, 082008. https://doi.org/10.1088/1742-6596/753/8/082008

Fourrière, A., Claudin, P., & Andreotti, B. (2010). Bedforms in a turbulent stream: Formation of ripples by primary linear instability and of dunes by nonlinear pattern coarsening. *Journal of Fluid Mechanics*, *649*, 287–328. https://doi.org/10.1017/S0022112009993466

Gao, X., Narteau, C., & Gadal, C. (2021). Migration of reversing dunes against the sand flow path as a singular expression of the speed-up effect. *Journal of Geophysical Research: Earth Surface*, *126*(5), e2020JF005913. https://doi.org/10.1029/2020JF005913

Guo, J. (2020). Empirical model for Shields diagram and its applications. *Journal of Hydraulic Engineering*, *146*(6), 04020038. https://doi.org/10.1061/(ASCE)HY.1943-7900.0001739

Hardy, R. J., Best, J. L., Marjoribanks, T. I., Parsons, D. R., & Ashworth, P. J. (2021). The influence of three dimensional topography on turbulent flow structures over dunes in unidirectional flows. *Journal of Geophysical Research: Earth Surface*, *126*(12), e2021JF006121. https://doi.org/10.1029/2021JF006121

Haugen, D. A., Kaimal, J. C., & Bradley, E. F. (1971). An experimental study of Reynolds stress and heat flux in the atmospheric surface layer. *Quarterly Journal of the Royal Meteorological Society*, *97*(412), 168–180. https://doi.org/10.1002/qj.49709741204

Ho, T. D., Valance, A., Dupont, P., & El-Moctar, A. O. (2011). Scaling laws in aeolian sand transport. *Physical Review Letters*, *106*(9), 094501. https://doi.org/10.1103/PhysRevLett.106.094501

Hunt, J. C. R., Leibovich, S., & Richards, K. J. (1988). Turbulent shear flows over low hills. *Quarterly Journal of the Royal Meteorological Society*, *114*(484), 1435–1470. https://doi.org/10.1002/qj.49711448405

Jackson, P. S., & Hunt, J. C. R. (1975). Turbulent wind flow over a low hill. *Quarterly Journal of the Royal Meteorological Society*, *101*(430), 929–955. https://doi.org/10.1002/qj.49710143015

Jenkins, J., & Valance, A. (2014). Periodic trajectories in aeolian sand transport. *Physics of Fluids*, *26*(7), 073301. https://doi.org/10.1063/1.4885576

Jia, P., Andreotti, B., & Claudin, P. (2023). Hydrodynamic roughness induced by a multiscale topography. *Journal of Fluid Mechanics*, *974*, A16. https://doi.org/10.1017/jfm.2023.795

Jimenez, J. A., Maia, L. P., Serra, J., & Morais, J. (1999). Aeolian dune migration along the Ceara coast, North-Eastern Brazil. *Sedimentology*, *46*(4), 689–701. https://doi.org/10.1046/j.1365-3091.1999.00240.x

Jin, T., Wang, P., & Zheng, X. (2021). Characterization of wind-blown sand with near-wall motions and turbulence: From grain-scale distributions to sediment transport. *Journal of Geophysical Research: Earth Surface*, *126*(8), e2021JF006234. https://doi.org/10.1029/2021JF006234

Kays, W. M., & Crawford, M. E. (1980). *Convection heat and mass transfer* (2nd ed.). McGraw-Hill.

Kiki-Sandoungout, S. (2019). *Caractérisation de la morphologie des dunes dans des écoulements unidirectionnels et alternatifs (Doctoral dissertation, Sciences de la Terre)*. Université de Bretagne Occidentale—Brest. Retrieved from https://tel.archives-ouvertes.fr/tel-02453140

Kroy, K., Sauermann, G., & Herrmann, H. J. (2002). Minimal model for sand dunes. *Physical Review Letters*, *88*(5), 054301. https://doi.org/10.1103/PhysRevLett.88.054301

Lane, S. N., Hardy, R. J., Elliott, L., & Ingham, D. B. (2004). Numerical modeling of flow processes over gravelly surfaces using structured grids and a numerical porosity treatment. *Water Resources Research*, *40*(1), W01302. https://doi.org/10.1029/2002WR001934

Launder, B., & Spalding, D. (1974). The numerical computation of turbulent flows. *Computer Methods in Applied Mechanics and Engineering*, *3*(2), 269–289. https://doi.org/10.1016/0045-7825(74)90029-2

Lefebvre, A., Paarlberg, A. J., & Winter, C. (2014). Flow separation and shear stress over angle-of-repose bed forms: A numerical investigation. *Water Resources Research*, *50*(2), 986–1005. https://doi.org/10.1002/2013WR014587

Liu, Y., Fang, H., Huang, L., & He, G. (2019). Numerical simulation of the production of three-dimensional sediment dunes. *Physics of Fluids*, *31*(9), 096603. https://doi.org/10.1063/1.5108741

Louge, M. Y., Valance, A., el Moctar, A. O., Xu, J., Hay, A. G., & Richer, R. (2013). Temperature and humidity within a mobile barchan sand dune, implications for microbial survival. *Journal of Geophysical Research: Earth Surface*, *118*(4), 2392–2405. https://doi.org/10.1002/2013JF002839

Louge, M. Y., Valance, A., Fang, J., & Porté-Agel, F. (2023). Data from: Evolution of turbulent boundary conditions on the surface of large barchan dunes: Anomalies in aerodynamic roughness and shear velocity, aeolian threshold and the role of dune skewness [Dataset]. *Cornell University Library*. https://doi.org/10.7298/6md9-1377

Louge, M. Y., Valance, A., Fang, J., & Porte-Agel, F. (2024). Data from: Evolution of turbulent boundary conditions on the surface of large barchan dunes: Anomalies in aerodynamic roughness and shear velocity, aeolian threshold and the role of dune skewness [Dataset]. *Cornell University Library*. https://doi.org/10.7298/6md9-1377.2

Louge, M. Y., Valance, A., Lancelot, P., Delannay, R., & Artières, O. (2015). Granular flows on a dissipative base. *Physical Review E*, *92*(2), 022204. https://doi.org/10.1103/PhysRevE.92.022204

Louge, M. Y., Valance, A., Xu, J., el Moctar, A. O., & Chasle, P. (2022). Water vapor transport across an arid sand surface—Non-linear thermal coupling, wind-driven pore advection, subsurface waves, and exchange with the atmospheric boundary layer. *Journal of Geophysical Research: Earth Surface*, *127*(4), e2021JF006490. https://doi.org/10.1029/2021JF006490

Lü, P., Dong, Z., & Rozier, O. (2018). The combined effect of sediment availability and wind regime on the morphology of aeolian sand dunes. *Journal of Geophysical Research: Earth Surface*, *123*(11), 1–9. https://doi.org/10.1029/2017JF004361

McEwan, I. K., & Willetts, B. B. (1993). Sand transport by wind: A review of the current conceptual model. *Geological Society, London, Special Publications*, *72*(1), 7–16. https://doi.org/10.1144/GSL.SP.1993.072.01.02

Michel, S., Avouac, J. P., Ayoub, F., Ewing, R. C., Vriend, N., & Heggy, E. (2018). Comparing dune migration measured from remote sensing with sand flux prediction based on weather data and model, a test case in Qatar. *Earth and Planetary Science Letters*, *497*, 12–21. https://doi.org/10.1016/j.epsl.2018.05.037

Michelsen, B., Strobl, S., Parteli, E. J., & Pöschel, T. (2015). Two-dimensional airflow modeling underpredicts the wind velocity over dunes. *Scientific Reports*, *5*, 1–8. https://doi.org/10.1038/srep16572

Moody, L. F. (1944). Friction factors for pipe flow. *Transactions of the American Society of Mechanical Engineers*, *66*(8), 671–678. https://doi.org/10.1115/1.4018140

Musa, R. A., Takarrouht, S., Louge, M. Y., Xu, J., & Berberich, M. E. (2014). Pore pressure in a wind-swept rippled bed below the suspension threshold. *Journal of Geophysical Research: Earth Surface*, *119*(12), 112–147. https://doi.org/10.1002/2014JF003293

Nakamura, N., & Tsuchiya, T. (2013). A model of regression lines through a common point: Estimation of the focal point in wind-blown sand phenomena. *Journal of Applied Statistics*, *40*(5), 1017–1031. https://doi.org/10.1080/02664763.2013.772570

Narteau, C., Zhang, D., Rozier, O., & Claudin, P. (2009). Setting the length and time scales of a cellular automaton dune model from the analysis of superimposed bed forms. *Journal of Geophysical Research*, *114*(F3), 1–18. https://doi.org/10.1029/2008JF001127

Nikuradse, J. (1933). *Strömungsgesetze in rauhen Rohren (laws of flow in rough pipes)* (pp. 1–62). NACA Technical Memorandum 1292. Retrieved from https://ntrs.nasa.gov/citations/19930093938

O'Brien, P., & Neuman, C. M. (2019). Experimental validation of the near-bed particle-borne stress profile in aeolian transport systems. *Journal of Geophysical Research: Earth Surface*, *124*, 1–12. https://doi.org/10.1029/2019JF005114

Omidyeganeh, M., & Piomelli, U. (2013). Large-eddy simulation of three-dimensional dunes in a steady, unidirectional flow. Part 1. Turbulence statistics. *Journal of Fluid Mechanics*, *721*, 454–483. https://doi.org/10.1017/jfm.2013.36

Pähtz, T., & Durán, O. (2018). The cessation threshold of nonsuspended sediment transport across aeolian and fluvial environments. *Journal of Geophysical Research: Earth Surface*, *123*(8), 1638–1666. https://doi.org/10.1029/2017JF004580

Pähtz, T., & Durán, O. (2023). Scaling laws for planetary sediment transport from DEM-RANS numerical simulations. *Journal of Fluid Mechanics*, *963*, A20. https://doi.org/10.1017/jfm.2023.343

Saph, A. V., & Schoder, E. W. (1903). An experimental study of the resistances to the flow of water in pipes. *Transactions of the American Society of Civil Engineers*, *51*(2), 253–312. https://doi.org/10.1061/TACEAT.0001608

Sauermann, G., Andrade, J. S. A., Jr., Maia, L. P., Costa, U. M. S., Araújo, A. D., & Herrmann, H. J. (2003). Wind velocity and sand transport on a barchan dune. *Geomorphology*, *54*(3–4), 245–255. https://doi.org/10.1016/S0169-555X(02)00359-8

Sauermann, G., Kroy, K., & Herrmann, H. J. (2001). Continuum saltation model for sand dunes. *Physical Review E*, *64*(3), 031305. https://doi.org/10.1103/PhysRevE.64.031305

Sauermann, G., Rognon, P., Poliakov, A., & Herrmann, H. J. (2000). The shape of the barchan dunes of Southern Morocco. *Geomorphology*, *36*(1–2), 47–62. https://doi.org/10.1016/S0169-555X(00)00047-7

Shields, A. (1936). *Application of similarity principles and turbulence research to bed-load movement, translated by W. P. Ott and J. C. van Uchelen*. USDA. Retrieved from https://authors.library.caltech.edu/25992/1/Sheilds.pdf

Smith, A. B., Jackson, D. W., & Cooper, J. A. G. (2017). Three-dimensional airflow and sediment transport patterns over barchan dunes. *Geomorphology*, *278*, 28–42. https://doi.org/10.1016/j.geomorph.2016.10.025

Smith, J. D. (1975). *Modeling of sediment transport on continental shelves* (pp. 1–83). Washington University Department of Oceanography.

Smyth, T. A. (2016). A review of computational fluid dynamics (CFD) airflow modelling over aeolian landforms. *Aeolian research*, *22*, 153–164. https://doi.org/10.1016/j.aeolia.2016.07.003

Sotiropoulos, F., & Khosronejad, A. (2016). Sand waves in environmental flows: Insights gained by coupling large-eddy simulation with morphodynamics. *Physics of Fluids*, *28*(2), 021301. https://doi.org/10.1063/1.4939987

Stoll, R., & Porté-Agel, F. (2006). Dynamic subgrid-scale models for momentum and scalar fluxes in large-eddy simulations of neutrally stratified atmospheric boundary layers over heterogeneous terrain. *Water Resources Research*, *42*(1), W01409. https://doi.org/10.1029/2005WR003989

Sun, Y., & Zheng, S. (2023). Large eddy simulation of atmospheric boundary flow over two two-dimensional hills. *Physics of Fluids*, *35*, 061701. https://doi.org/10.1063/5.0154416

Swann, C., Sherman, D., & Ewing, R. (2020). Experimentally-derived thresholds for windblown sand on Mars. *Geophysical Research Letters*, *47*(3), e2019GL084484. https://doi.org/10.1029/2019GL084484

Taylor, P. A., Mason, P. J., & Bradley, E. F. (1987). Boundary-layer flow over low hills. *Boundary-Layer Meteorology*, *39*(1–2), 107–132. https://doi.org/10.1007/bf00121870

Tsinontides, S., & Jackson, R. (1993). The mechanics of gas fluidized beds with an interval of stable fluidization. *Journal of Fluid Mechanics*, *255*(1), 237–274. https://doi.org/10.1017/S0022112093002472

Walmsley, J. L., A.Taylor, P., & Keith, T. (1986). A simple model of neutrally stratified boundary-layer flow over complex terrain with surface roughness modulations (MS3DJH/3R). *Boundary-Layer Meteorology*, *36*(1–2), 157–186. https://doi.org/10.1007/BF00117466

Weaver, C., & Wiggs, G. (2011). Field measurements of mean and turbulent airflow over a barchan sand dune. *Geomorphology*, *128*(1–2), 32–41. https://doi.org/10.1016/j.geomorph.2010.12.020

Weng, W., Hunt, J., Carruthers, D., Warren, A., Wiggs, G., Livingstone, I., & Castro, I. (1991). Air flow and sand transport over sand-dunes. In O. E. Barndorff-Nielsen & B. B. Willetts (Eds.), *Aeolian grain transport: The erosional environment* (Vol. 2, pp. 1–22). Springer-Verlag. https://doi.org/10.1007/978-3-7091-6703-8_1

Wu, X., & Moin, P. (2009). Direct numerical simulation of turbulence in a nominally zero-pressure-gradient flat-plate boundary layer. *Journal of Fluid Mechanics*, *630*, 5–41. https://doi.org/10.1017/S0022112009006624

Wyngaard, J. C. (2010). *Turbulence in the atmosphere*. Cambridge University Press.

Xiao, X., Liu, H., & Zheng, X. (2023). Temporal evolution of dune number density in a barchan dune field. *Journal of Geophysical Research: Earth Surface*, *128*(5), e2022JF007036. https://doi.org/10.1029/2022JF007036

Zhang, D., Narteau, C., & Rozier, O. (2010). Morphodynamics of barchan and transverse dunes using a cellular automaton model. *Journal of Geophysical Research*, *115*(F3), F03041. https://doi.org/10.1029/2009jf001620

Zhang, D., Narteau, C., Rozier, O., & du Pont, S. C. (2012). Morphology and dynamics of star dunes from numerical modelling. *Nature Geoscience*, *5*(7), 463–467. https://doi.org/10.1038/ngeo1503

Zhang, Q., Deal, E., Perron, J. T., Venditti, J. G., Benavides, S. J., Rushlow, M., & Kamrin, K. (2022). Fluid-driven transport of round sediment particles: From discrete simulations to continuum modeling. *Journal of Geophysical Research: Earth Surface*, *127*(7), e2021JF006504. https://doi.org/10.1029/2021JF006504

Zheng, X., Jin, T., & Wang, P. (2020). The influence of surface stress fluctuation on saltation sand transport around threshold. *Journal of Geophysical Research: Earth Surface*, *125*(5), e2019JF005246. https://doi.org/10.1029/2019JF005246

Zhu, W., Huo, X., Zhang, J., Wang, P., Pähtz, T., Huang, N., & He, Z. (2019). Large effects of particle size heterogeneity on dynamic saltation threshold. *Journal of Geophysical Research: Earth Surface*, *124*(8), 1–11. https://doi.org/10.1029/2019JF005094